DISSERTATIONES CHIMICAE UNIVERSITATIS TARTUENSIS
**86**

DISSERTATIONES CHIMICAE UNIVERSITATIS TARTUENSIS
**86**

**JAANUS ESKUSSON**

# Synthesis and characterisation of diamond-like carbon thin films prepared by pulsed laser deposition method

TARTU UNIVERSITY
PRESS

This study was carried out at the Institute of Chemistry and at the Institute of Physics, University of Tartu, Estonia.

Dissertation is accepted for the commencement of the degree of Doctor of Philosophy in Chemistry on May 20, 2009, by the Doctoral Committee of the Institute of Chemistry, University of Tartu.

| | |
|---|---|
| Supervisors: | Prof. Enn Lust and Dr. Raivo Jaaniso,<br>University of Tartu, Estonia |
| Opponents: | Prof. Lauri Niinistö,<br>Helsinki University of Technology, Finland |
| Commencement: | $15^{30}$ June 25 2009, in Tartu, 18 Ülikooli Str.,<br>in the University council hall |

ISSN 1406–0299
ISBN 978–9949–19–129–1 (trükis)
ISBN 978–9949–19–130–7 (PDF)



Tartu Ülikooli Kirjastus
www.tyk.ee
Tellimus nr. 187

# CONTENTS

# I. LIST OF ORIGINAL PUBLICATIONS

**I.** **J. Eskusson**, R. Jaaniso, T. Avarmaa, T. Jantson, E. Lust, Synthesis of diamond-like carbon films by pulsed laser deposition in a tiny vacuum chamber, SPIE Proceedings, 6591 (2007) 65910L/1.

**II.** **J. Eskusson**, R. Jaaniso, E. Lust, Synthesis of DLC films by PLD from liquid target and dependence of film properties on the synthesis conditions, Appl. Phys. A, (2008) 745.

**III.** **J. Eskusson**, R. Jaaniso, E. Lust, Diamond-like phase formation in an amorphous carbon films prepared by periodic pulsed laser deposition and laser irradiation method, Appl. Surf. Sci., 255 (2009) 7104.

**IV.** G. Nurk, **J. Eskusson**, R. Jaaniso, E. Lust, Electrochemical properties of diamond-like carbon electrodes prepared by pulsed laser deposition method, J. Solid State Electrochem., 7 (2003) 421.

### Author's contribution

The author performed all carbon films synthesis, constructed pulsed laser deposition chamber and composed synthesis setup (I, II, III, IV). The author performed all carbon films optical, Raman scattering spectroscopy, atomic force microscopy and thickness measurements (I, II, III, IV)

The author is responsible for all modelling, interpretations and writing of the articles (I, II, III).

The author participated in the carbon films characterizations and article preparation (IV).

# 2. ABBREVIATIONS AND SYMBOLS

| | |
|---|---|
| $A$ | constant characterizing the permittivity of a solvent ($A = (2\varepsilon\varepsilon_0 RT)^{-1/2}$) |
| $A_1$ | high-frequency constant phase element coefficient |
| $A_2$ | low-frequency constant phase element coefficient |
| a-C | amorphous carbon |
| AFM | atomic force microscopy |
| $C$ | differential capacitance |
| CCD | charge couple device |
| CPE | constant phase element |
| $CPE_1$ | high-frequency constant phase element |
| $CPE_2$ | low-frequency constant phase element |
| $C_{ad}$ | adsorption capacitance |
| $C_b$ | total capacitance |
| $C_{dl}$ | electrical double layer capacitance |
| $C_{ext}$ | external capacitance |
| $C_p$ | parallel differential capacitance |
| $C_s$ | series differential capacitance |
| $C_1$ | high frequency capacitance |
| $C_2$ | meium frequency capacitance |
| $C_3$ | low frequency adsorption capacitance |
| CV | cyclic voltammograms |
| $D$ | effective diffusion coefficient of a particle |
| DLC | diamond-like carbon |
| DLCE | diamond-like carbon electrode |
| $E$ | electrode potential |
| EELS | electron energy loss spectroscopy |
| $f$ | alternative current frequency |
| GFW | generalized finite-length Warburg element |
| $h_f$ | thickness of a diamond-like carbon film with resistance $R_3$ |
| $I_D$ | D-band integral intensity |
| $I_G$ | G-band integral intensity |
| j | imaginary unit (j = $\sqrt{-1}$) |
| $j$ | current density |
| $L$ | effective diffuse layer thickness |
| NPCE | nanoporous carbon electrode |
| PLD | pulsed laser deposition |
| $R_{ad}$ | charge transfer resistance |
| $R_b$ | total resistance of the bulk electrolyte |
| $R_d$ | diffusion resistance |
| $R_{dl}$ | electrical double layer resistance |
| $R_{el}$ | high-frequency resistance of the electrode system |
| $R_{ext}$ | external resistance |

| | |
|---|---|
| $R_p$ | parallel charge transfer resistance |
| RMS | root mean square roughness |
| $R_s$ | series charge transfer resistance |
| $R_1$ | charge transfer resistance of the flat electrode\|solution interface |
| $R_2$ | partial charge transfer resistance at the internal surfaces for a rough electrode |
| $R_3$ | surface film resistance |
| $T$ | frequency parameter ($T=L^2/D$) |
| ta-C | tetrahedral amorphous carbon |
| $v$ | electrode potential scan rate |
| $v_{\max}^{If}$ | characteristic frequency of the low frequency process (ie. - Z``, Z´ - plot maximum of frequencies $f < 1$ Hz) |
| $v_1$, $v_2$ | rates of the reactions 1 and 2 |
| Z´, jZ`` | active and imaginary parts of the impedance |
| $Z_{ext}$ | external impedance |
| $Z_{GFW}$ | generalized Warburg-like diffusion impedance |
| $Z_W$ | Warburg-like diffusion impedance |
| α, $\alpha_1$, $\alpha_2$ | transfer coefficients |
| $\alpha_w$, | fractional exponent of Warburg-like diffusion impedance |
| $\varepsilon$ | dielectric constant of the solvent |
| $\varepsilon_f$ | dielectric constant of the film |
| $\delta$ | phase angle |
| σ | surface charge density |
| λ | (ac) alternative current penetration depth |
| $\tau_{\max}$ | characteristic relaxation time |
| $\tau_{\max}^{If}$ | characteristic relaxation time in the low frequency region |
| $\Delta^2$ | weighted sum of the squares |
| $\chi^2$ | chi-square function |
| $\omega$ | angular frequency (equal to $2\pi f$) |

# 3. INTRODUCTION

Carbon has mainly two allotropic forms: graphite and diamond widely used in modern technology including lithium ion batteries, electrical double layer supercapacitors and as electrodes for electroanalysis and electrosynthesis reactors, respectively. Diamond-like carbon (DLC) films can be deposited using several different techniques leading to a variety of different properties of the films. Pulsed laser deposition (PLD) has proved to be an effective technique for deposition of a wide variety of thin film materials, including DLC, oxides and various nanostructured materials [1]. In the past decade, PLD process has become popular for its ability to generate highly energetic carbon species which enhances the formation of high percentage of $sp^3$ bonded carbon atoms at low substrate temperatures and, therefore, deposition of high quality DLC film can be realized [2]. In PLD process a laser beam is focused onto a target to evaporate its surface layer. The vaporized material – consisting of atoms, ions and atomic clusters – is then deposited onto the substrate, which is mounted opposite to the target, in the vacuum chamber [3]. PLD technique is characterized by low deposition temperatures and high deposition rates. The ratio of $sp^3/sp^2$ carbon atoms in diamond-like films depends on process parameters, such as type and pressure of the reagent gas, substrate temperature, laser wavelength and power density [4].

The main aim of this work was to determine carbon films properties dependence on the synthesis parameters, especially on the substrate irradiation conditions. To date, most fundamental research on carbon structures has been focused on their growth mechanism [5, 6]. Initiated from our further goal – to synthesize wide bandgap DLC films, which contain new types of dopants, liquid source of substances was used as a target material. Liquid target material permits relatively simply to add some (rare earth) metal dopant to this and simplify synthesis setup configuration noticeable. These kinds of materials may open new interesting possibilities for the applications in optics, electrochemistry and in other fields of science and modern technology.

For electrochemical applications, polycrystalline diamond-like carbon electrodes (DLCEs) were prepared by PLD method and the impedance and cyclic voltammetry characteristics for the DLCE|*x*M NaF aqueous solution interface were established.

# 4. LITERATURE OWERVIEW

Carbon has mainly two allotropic forms: graphite and diamond. In graphite the carbon atoms are in $sp^2$ hybridization and in diamond they are in $sp^3$ hybridization. At normal pressure and temperature diamond is thermodynamically unstable compared to graphite, but mechanically stronger [7]. Diamond exhibits several remarkable properties of technological interest: it is very dense and extremely hard, has a large thermal conductivity and has free carriers with a high mobility [8–25]. Experimental evidence suggests that well over 80% of the atoms in amorphous carbon (a-C, intermediate form between the diamond and graphite) thin film are in $sp^2$ hybridization [26]. The disordered a-C can be imagined like the $sp^2$ hybridized carbon clusters are embedded in the $sp^3$ hybridized carbon matrix [27]. Interest in a-C is due to its room-temperature growth, thermal stability and diamond-like tribological properties [28, 29]. DLC films, also known as tetrahedral a-C films, usually contain a relatively high proportion of $sp^3$-hybridized carbon atoms together with $sp^2$ hybridized carbon bonds.

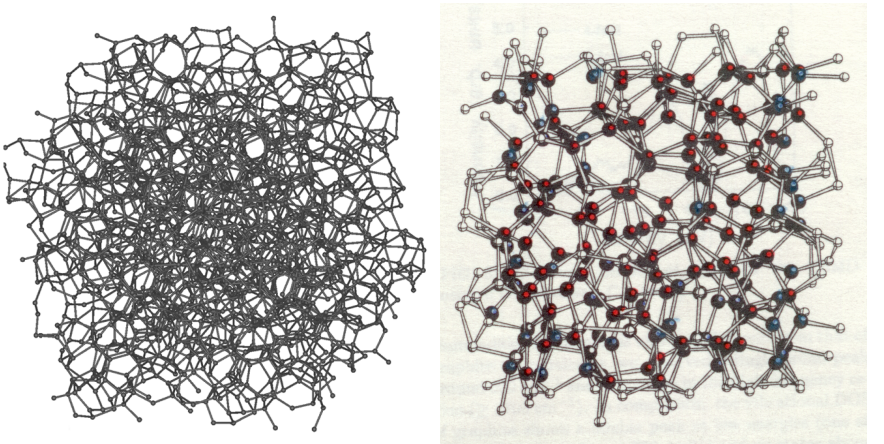

**Figure 1.** Different ball and stick models of a-C.

Such bonding structure results in unique combination of DLC properties, as extremely high hardness, low friction coefficient, high wear-resistance, excellent chemical stability, good thermal conductivity and good transparency in the IR region. DLC has been an interesting subject of research over the last two decades [30–34]. Thin films of this material exhibit a wide range of mechanical, electronic, electro-chemical and antimicrobial properties. They are very suitable for applications involving the formation of protective coatings for mechanical tools and magnetic recording disks, optical devices, field emission components

for vacuum microelectronics as well as in medicine for biocompatible implants and coatings for other medical devices [32, 35–38].

Raman spectroscopy is a very sensitive tool for observing the degree of structural disorder and the type of chemical bond. Therefore Raman spectroscopy is one of the most widely applied methods for the structural analysis of the carbon films. Graphite, diamond and diamond-like carbon have all distinctive Raman spectra.

Graphite has one Raman-active vibration – the C-C stretching mode wavenumber of which is 1581 $cm^{-1}$ and which is referred as the G band in the Raman spectrum. If the carbon structure involves disorder, then the G band width characterizes the degree of disorder in the layer of graphite, and the G band shift towards lower wavenumber indicates increasing of the $sp^3$-hybridized carbon content. In disordered structure or in small-grain polycrystalline graphite, a second Raman line (referred as the D band) appears at a lower wavenumber between the 1350 and 1357 $cm^{-1}$. This is caused by the breakdown of a Raman scattering selection rule and gives useful information about the degree of carbon disordering [39, 40].

Diamond has one Raman-active vibration at wavenumber 1332 $cm^{-1}$. The Raman scattering cross-section of this line is 50 times smaller than the corresponding cross-section of graphite G band. Therefore, if the intensities of diamond line and G band are similar in the spectra, then one may expect that there are nearly 50 times more $sp^3$ hybridized carbon atoms than $sp^2$ hybridized ones in DLC.

The Raman spectrum of DLC represents a relatively wide and complex band, which consists of many subbands between the D and the G bands. Although DLC does not have its own specific narrow Raman line, these spectra are clearly distinctive from other carbon forms and this confirms the idea that DLC has self-containing structure [39]. Usually, in literature, two types of DLC spectra are given. The first type of DLC spectra consist of two lines, where the smaller frequency line is situated near 1390 $cm^{-1}$ (D band), and a second line is situated near 1546 $cm^{-1}$ (G band) [41]. The second kind of DLC spectra consist of a wide band with the maximum situated from 1460 to 1540 $cm^{-1}$, depending on DLC preparation, and on the ratio of carbons in $sp^2/sp^3$ hybridization states [39, 42, 43].

It should be noted that different interpretations of Raman spectra for amorphous carbon film structures and corresponding structural changes were discussed in literature [39–44]. The existence of a D peak indicates the presence of aromatic carbon rings. The G band for carbon materials arises from vibrations of all $sp^2$ sites and in both chain or ring configurations. The intensity of a D band however arises only from clusters of $sp^2$ sites in six fold aromatic rings [45–47]. Smaller aromatic clusters have higher modes and shift D band upwards [46]. It was noted that G band shifting to the higher frequencies is in good correlation with increasing content of $sp^2$ hybridized carbon content in the film [45, 46]. In figure 2 we can see Schematic diagram of influences on the Raman spectra.

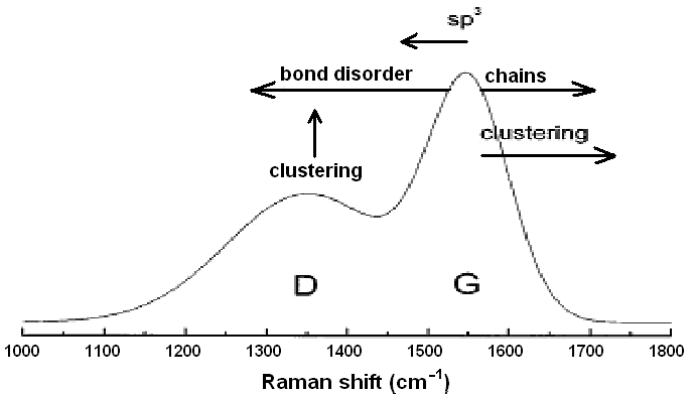


**Figure 2.** Schematic diagram characterising the influence of bonding type and clustering on the Raman spectra.

Theoretical calculations predict that the electronic properties of carbon forms will be variable over very wide limits. Interest in nanostructured carbon electrodes is caused by their unique geometrical, mechanical, electronic and chemical properties. DLCEs have been objects of very many fundamental and applied studies, but the electrochemical characteristics of the material are not very well established [5, 6, 8–25, 48–58]. Diamond is an insulator with a band gap of ~5.5 eV. However, p-type conductivity and semi-metallic behaviour can be achieved by boron incorporation [8–10, 13, 20, 23, 25]. Usually, the highly boron-doped diamond thin film electrodes were deposited on various conductive substrates, using microwave-assisted plasma-enhanced chemical vapor deposition and other similar methods [5, 8–13, 19, 20, 23 48–56]. Highly doped diamond is an interesting electrode material for fundamental electrochemistry studies, including the kinetics and mechanism of electron transfer processes. The excellent chemical inertness, combined with a low background current density and the large potential range between the onset of oxygen and hydrogen evolution, favour the use of diamond for the electroanalysis of a variety of electroactive species [13, 20, 48–51]. Differently from many semiconductors and metals, diamond does not form a macroscopic oxide layer on its surface and it does not dissolve anodically (oxidize) or cathodically over a very wide potential region (~3.0 V) [51].

Electrochemical impedance studies show the very high capacitance values for polycrystalline diamond electrodes [8, 20, 21, 51, 52, 57]. Electrodes from good quality material with a faceted surface have a smaller interfacial capacitance than those from materials with polycrystalline (fractal or porous) surface morphology and surface regions, consisting of carbon in the $sp^2$ hybridization state [8, 13, 23, 50–56]. In some cases, the results indicated that the interfacial capacitance is determined by a majority carrier depletion layer and the capacitance versus voltage plot agrees with the Mott-Schottky relationship over a limited potential region [8–10, 13, 20, 24, 25, 52–56].

# 5. EXPERIMENTAL

In this work, carbon thin films synthesis by PLD have been studied. Although different types of experimental setup have been used in films synthesis, the laser wavelength (248 nm) and the target material was same for all depositions, only substrate material was different in some depositions. Applied laser was KrF eximer laser (ESTLA EXC-150/25) which produced 25 ns pulses with maximum energy of 250 mJ. All experiments had the laser beam intensity regulating computer-controlled system.

For all synthesis the target material was a vacuum oil Santovac-5 [59–61]. This oil has very low vapor pressure ($P^{20°C} = 2.6\times10^{-10}$ mbar) and very high absorption coefficient at our laser wavelength 248 nm (Fig. 3).

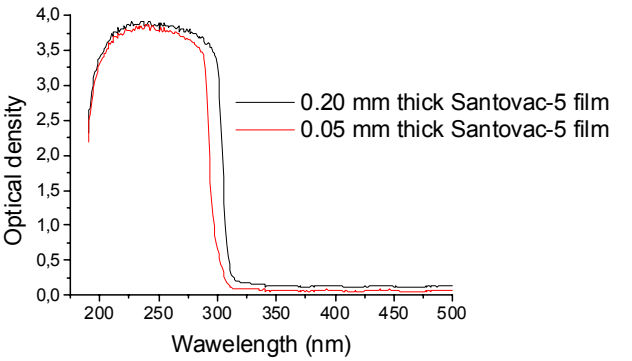


**Figure 3.** Absorption spectra of Santovac-5 at different thicknesses.

According to the Beer-Lambert law (equation 1).

$$\chi l = \log I_0 - \log I$$
$$\chi l = D, \tag{1}$$

where $I$ is the light intensity after passing through the sample, $I_0$ – initial light intensity, $\chi$ – absorption coefficient, $l$ – thickness of the sample, $D$ – optical density. From equation (1) we can see that when the material layer thickness increases, the optical density must increase linearly, too. In figure 3 we clearly see that optical density stays practically the same, when Santovac-5 layer thickness increases from 0.05 mm to 0.2 mm. This means that Santovac-5 has very high optical density already in a relatively thin layer of Santovac-5 and, therefore, the permeating signal from a sample decreases so much that the spectrometer is not able to detect it.

Experimental studies in this work can be divided into four groups. First group is synthesis of thin carbon films by PLD in a very miniature vacuum

chamber. In second group, depositions and substrate laser excitations were carried out at the same time by semitransparent mirror applied. In third group of carbon films synthesis, the applied laser was operating periodically between the deposition and excitation pulses by the movable mirror used. Fourth group carbon films synthesis is related to the studies for electrochemical applications.

All Raman scattering spectra were recorded by a double diffraction grating spectrometer (SPEX 1402) and the detection unit was a photo-multiplier operating in a photon counting mode or a cooled CCD camera (Andor, model DU420-BU). Excitation light source for Raman analyses was an Ar-laser with 488 nm wavelength. Film surface microstructure studies were performed by an AFM in contact (Autoprobe CP) or noncontact (Agilent Technologies 5500 measurement system) mode regime. Thickness measurements were performed by the Dektak IIA instrument with 25 μm tip and 2 mm scan rate. The thicknesses of films deposited were mostly lower than 200 nm. All DLC film measurements were made at room temperature.

## 5.1. Thin carbon films synthesis by PLD in miniature vacuum chamber

The scheme of the PLD system setup for DLC thin film synthesis is shown in figure 4. All depositions were carried out in an extremely small vacuum chamber at room temperature and at pressures ranging from $2\times10^{-5}$ to $2\times10^{-3}$ bar. The main objective at designing the chamber was to take the maximum advantage from the nonequilibrium character of pulsed laser deposition and from the high energy of ablated material in this process. The chamber allowed performing efficient combinatorial synthesis of the films, as the materials irradiated with different doses of laser energy were grown simultaneously during a single deposition process. The DLC film deposition equipment was composed of the KrF eximer laser, a laser beam intensity regulating system; optical components; a pumping system with valves; a very small reaction chamber; and $H_2O_2$ reservoir.

In our experiment Santovac-5 is situated at the bottom of the very miniature (inside volume below 1 $cm^3$) reaction chamber (ablation chamber, Fig. 5), where distance between the target and the substrate was 10 mm. The reaction chamber was closed at the top by a fused silica window (1×8×15 mm) onto the inner surface of which the DLC film was expected to deposit. Since the chamber window and the deposition substrate was the same, at every laser pulse the already deposited DLC film was irradiated by a nonfocused laser beam (laser spot size ~3×8 mm), which excited and supported the DLC structure formation. The reaction chamber has two connection tubes: one tube connects the chamber with vacuum pumps; and the second tube, opposite the first tube, connects the chamber with a $H_2O_2$ reservoir. Through the valve between the $H_2O_2$ reservoir and the reaction chamber we could adjust the amount of $H_2O_2$ vapor into the reaction chamber. It should be noted that in literature there is no detailed mechanism explaining influence of $H_2O_2$ vapor on the $sp^3$-hybridized

carbon formation process, however there are some experimental reports demonstrating the influence of $H_2O_2$ vapor on the DLC film formation process [61].

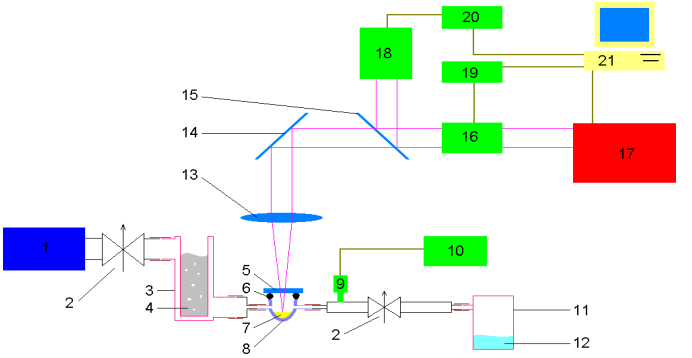


**Figure 4.** Schematic representation of DLC films synthesis (setup No. 1). 1 – vacuum pump, 2 – valve, 3 – liquid $N_2$ reservoir, 4 – liquid $N_2$, 5 – substrate (window), 6 – o-ring seal, 7 – vacuum oil, 8 – reaction chamber, 9 – vacuum gauge, 10 – controller, 11 – $H_2O_2$ reservoir, 12 – $H_2O_2$, 13 – lens, 14 – mirror, 15 – semitransparent mirror, 16 – regulator of laser beam intensity, 17 – excimer laser (248 nm), 18 – pyroelectric laser pulse energy meter, 19 – step-motor driver, 20 – analogue-digital converter, 21 – PC.

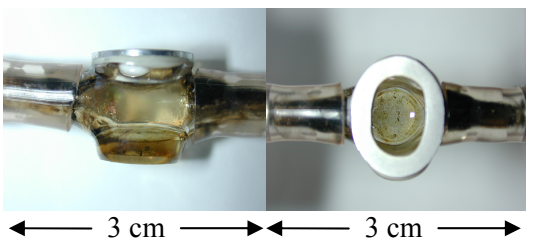


**Figure 5.** Side and top view of reaction chamber.

Through the optical components and reaction chamber window we drove a laser beam and created a laser beam spot of about 0.5 – 1 $mm^2$ on the ablation target (Fig. 4). Laser beam intensity was feedback-fixed, and 16 – 35 mJ of energy (1.6 – 7 $J/cm^2$) per pulse got through onto the ablation target.

Our pumping system consists of two pumps: the first pump is a prevacuum rotor pump, and the second one is a liquid $N_2$ cryogenic pump (Fig. 4). Before the experiment the vacuum oil was vacuumed to remove the dissolved gases. The system was vacuumed firstly by rotor pump, and after the base vacuum was achieved, with the aid of the liquid $N_2$ cryogenic pump. After the base vacuum was achieved, the reagent gas valve was opened to a fixed rate, let to stabilize for 20 minutes and then the deposition process was started. All deposition parameters are listed in table 1.

**Table 1.** Synthesis parameters of DLC.

| Film No. | Laser frequency | Energy of laser pulse | Base vacuum | Valve position | Deposition vacuum | Number of pulses |
|---|---|---|---|---|---|---|
| 1 | 2 Hz | 16 mJ | 0.076 mbar | 0 | 0.073 mbar | 8000 |
| 2 | 5 Hz | 16 mJ | 0.035 mbar | 11 | 1.112 mbar | 2000 |
| 3 | 5 Hz | 16 mJ | 0.014 mbar | 7 | 1.145 mbar | 2000 |
| 4 | 5 Hz | 16 mJ | 0.019 mbar | 4 | 0.026 mbar | 2000 |
| 5 | 5 Hz | 25 mJ | 0.015 mbar | 9.5 | 1.145 mbar | 2000 |
| 6 | 5 Hz | 35 mJ | 0.014 mbar | 8 | 1.112 mbar | 2000 |
| 7 | 5 Hz | 35 mJ | 0.017 mbar | 10 | 1.145 mbar | 510 |

The prepared DLC films were characterized by optical microscopy, Raman scattering spectroscopy and AFM.

## 5.2. Semitransparent mirror assisted thin carbon films deposition with laser substrate excitation

The scheme of the PLD system setup for DLC thin film synthesis is shown in figure 6. All depositions were carried out at temperatures from 18 to 600°C and pressures from $4\times10^{-7}$ to $2\times10^{-3}$ bar. The DLC film deposition equipment was composed of the KrF eximer laser; a computer controlling unit; optical components; a pumping system; reaction chamber; and $H_2O_2$ reservoir.

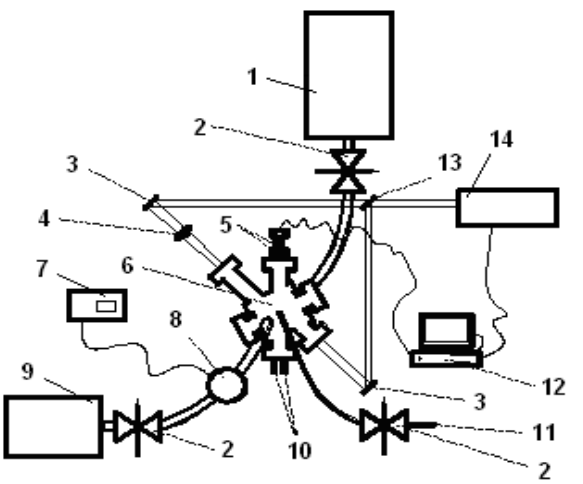


**Figure 6.** Schematic representation of DLC films synthesis (setup No. 2). 1 – He cryogenic pump, 2 – valve, 3 – mirror, 4 – lens, 5 – heater and thermocouple connection, 6 – deposition chamber, 7 – controller, 8 – vacuum gauge, 9 – vacuum pump, 10 – target cooling tubes, 11 – reagent gas ($H_2O_2$) inlet, 12 – PC, 13 – semitransparent mirror, 14 – excimer laser (248 nm).

Ablation source (target) was a vacuum oil Santovac-5 and in this experiment it (1 mm thick layer) situated at the bottom of the cooling target holder and was previously vacuumed from dissolved gases. The distance between the target and the substrate was 4 cm. Fused silica plates (1×10×10 mm) were used as substrates which were cleaned firstly mechanically, thereafter, cleaned for 10 minutes in a sonic bath with acetone, and after that rinsed with ethanol and methanol.

The deposition chamber has three connection tubes (Fig. 6): one tube connects the chamber with the He cryogenic pump; the second tube, opposite to the first tube, connects the chamber with an $H_2O_2$ reservoir and the third tube is for the pre-vacuum pump. Connection of the pre-vacuum pump was closed before the beginning of the deposition process and the cryogenic pump was used during the deposition process. The amount of $H_2O_2$ vapor entering the deposition chamber was controlled through the valve between the $H_2O_2$ reservoir and the deposition chamber. The level of base vacuum (before the reagent gas valve was opened) was up to $10^{-6}$ mbar.

Before entering the deposition chamber, the applied laser beam has been divided by the semitransparent (50%) mirror into two parts (Fig. 6). One part of the divided laser beam was focused by the quarts lens on the liquid target with a spot size of ~1.5 $mm^2$, and the second, nonfocused laser beam irradiated at the same time the growing DLC film on the silica substrate (laser beam cross-section area on the substrate was 5×12 mm). It Based on our previous experimental studies, where a noticeable influence of the laser irradiation on the content of carbon in $sp^3$-hybridization state in DLC films has been observed, it was assumed that the laser activation could be very useful for DLC formation process. Laser pulse frequency was all the time 10 Hz and the laser beam energy was varied from 20 to 130 mJ (1.3 – 8.7 J/$cm^2$) per pulse to the ablation target.

The prepared DLC films were characterized by AFM and Raman scattering spectroscopy.

## 5.3. Movable mirror assisted thin carbon films interval deposition with laser substrate excitation

For DLC film synthesis PLD system was used, which provided possibility for interval deposition, whereas the films were irradiated by the laser pulses between the deposition intervals. The main difference of experimental setup from our two previous systems (deposition and substrate excitation were carried out by the same laser pulse) was that this system allowed not simultaneous but sequential excitation between the deposition pulses. The scheme of the PLD system setup is shown in figure 7.

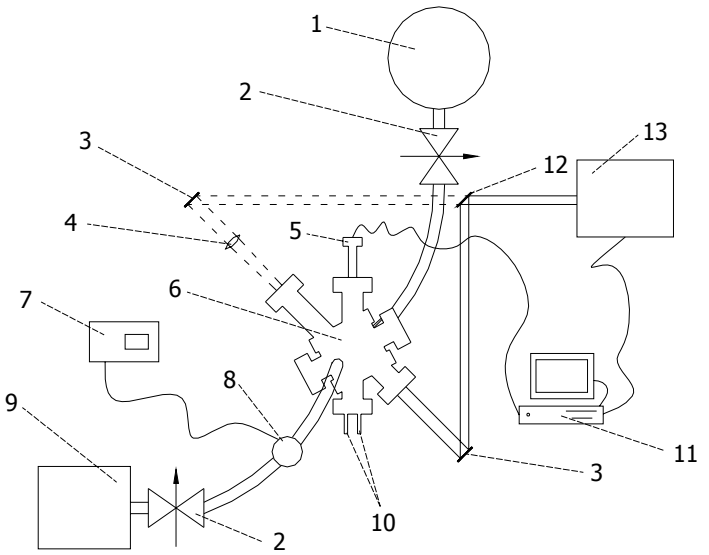


**Figure 7.** Schematic representation of DLC film synthesis (setup No. 3). 1 – He cryogenic pump, 2 – valve, 3 – mirror, 4 – lens, 5 – temperature sensor connection, 6 – deposition chamber, 7 – controller, 8 – vacuum gauge, 9 – vacuum pump, 10 – target cooling tubes, 11 – PC, 12 – periodically movable mirror, 13 – excimer laser (248 nm).

This modification gives us an opportunity to vary the substrate excitation parameters (number, frequency and intensity of the laser pulses) separately from the target ablation parameters. All depositions were carried out at temperatures from 28 to 36°C and at pressures from $2\times10^{-3}$ to $9\times10^{-3}$ mbar. The DLC film deposition equipment was composed of the KrF eximer laser; laser beam intensity and moving controlling system, needful optical components and a pumping system; as well as from reaction chamber (Fig. 7).

A vacuum oil Santovac-5 was used as the ablation source. In this experiment Santovac-5 (1 mm thick layer) was situated at the bottom of the target holder and was previously vacuumed to separate the dissolved gases. The distance between the target and the substrate was 4 cm. Fused silica plates (1×10× 10 mm) were used as substrates, cleaned firstly mechanically and thereafter during 10 minutes in a sonification bath filled with acetone. After surface treatment silica plates were rinsed with ethanol and methanol.

The deposition chamber has two connection tubes (Fig. 7): first one connects the chamber with the He cryogenic pump and the second tube connects the pre-vacuum pump to the vacuum chamber. Connection of the pre-vacuum pump was closed before the beginning of the deposition process and the cryogenic pump was used during the deposition process.

Applied laser beam was focused by the quarts lens onto the liquid target with a spot size of ~2 $mm^2$. Some laser beam pulses were guided to the growing DLC film on the silica substrate by the movable mirror (Fig. 7). The frequency,

quantity and intensity of the deposition and excitation laser pulses were separately tunable. For most of a-C samples (Raman spectra are given in Fig. 16) the following deposition regime was applied: after three ablation pulses (energy density 5 J/cm$^2$ and frequency f=5 Hz) one activation (substrate irradiation with fixed intensity from 4 to 100 mJ for different samples) pulse has been used and in total one thousand cycles has been made. For some DLC films (Raman spectrum is given in Fig. 17) somewhat different deposition regime has been used: after three ablation pulses (5 J/cm$^2$ and f = 5 Hz) 10 activation (substrate irradiation) pulses (with 100 mJ intensity and 25 Hz frequency) have been made. Excitation laser beam cross-section area on the substrate was 5×12 mm. It was not completely homogeneous and some scattering in surface energy density was observed.

For comparison, some carbon films were deposited under the same ablation conditions but without substrate irradiation. The prepared carbon films were characterized by AFM and Raman scattering spectroscopy method.

## 5.4. Synthesis of thin carbon films for electrochemical studies

The scheme of the PLD chamber for the DLCE synthesis is shown in figure 8. Experimental setup is similar like it is shown in figure 7, but without movable mirror for substrate excitation.

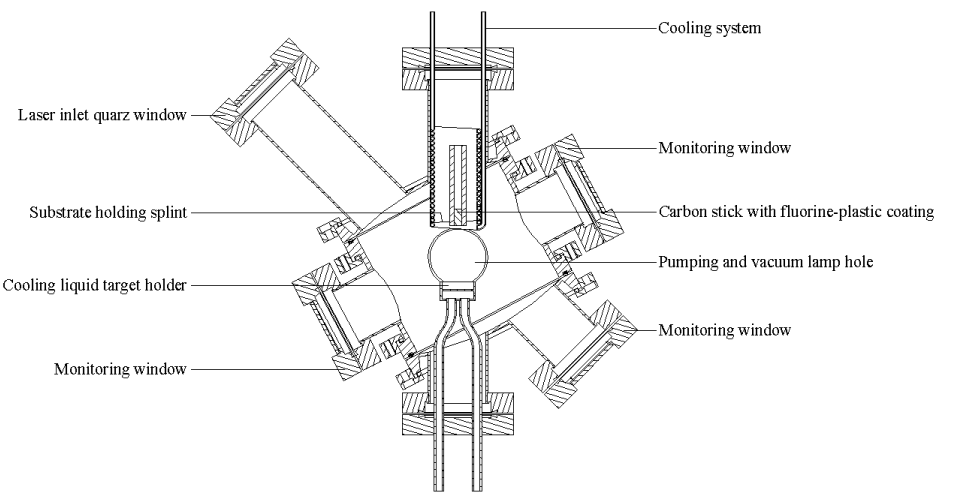


**Figure 8.** Scheme of the PLD chamber in the synthesis setup No. 4.

The KrF eximer laser beam with an energy density of 8.5–9.0 J $cm^{-2}$ was focused onto the liquid target at an angle of 45°. The target material was the vacuum pump oil Santovac 5. The ablated material was deposited onto the tip of a glassy carbon cylinder with the dimensions ∅5×10 mm, which was surrounded on the lateral sides by a polystyrene film and additionally isolated by a Teflon holder [6, 62–65]. The glassy carbon substrates (CY-2500) were fixed with a stainless steel splint, which permitted easy exchange of the substrates and use of different target-substrate distances, but mainly a 40 mm distance was used in the present experiment under discussion.

Before being inserted into the vacuum chamber, the substrates were mechanically polished, cleaned with concentrated HF and $HClO_4$ [9], washed using MilliQ+ water and ethanol and thereafter rinsed with methanol.

The base pressure inside the deposition chamber was ~$10^{-6}$ mbar. Deposition was carried out at room temperature with the following laser ablation parameters: pulse frequency, 10 Hz; spot area, ~1.5 $mm^2$; maximal number of pulses used was 1000.

The prepared DLC films were characterized by AFM and Raman scattering spectroscopy.

The electrical double layer impedance was measured using an Autolab PGSTAT 30 with a FRA 2 analyzer in the range of ac frequencies from 0.01 to 104 Hz with ±5 mV modulation. NaF for preparing the solutions was purified by triple recrystallization from MilliQ+ water and treated in vacuum to dryness. NaF was calcined at 700°C immediately prior to the preparation of the solutions. Pure Ar (99.9999%; from AGA) was bubbled for 1–2 h through the electrolyte before the submersion of the DLCE into the solution. The temperature was kept at 298 K. An AgCl|Ag (sat. KCl in $H_2O$) reference electrode was used and all the potentials are presented with respect to this reference electrode [6, 17–19, 57].

# 6. RESULTS AND DISCUSSION

## 6.1. Optical microscopy data

Due to nonhomogeneous irradiation of the growing films by a laser beam during the deposition process (Fig. 4), different DLC film areas on the fused silica substrate appear (Fig. 9). Firstly, one can divide these film areas into two regions: films which were grown outside the laser beam irradiated region and films which were grown inside the laser beam irradiated region.

Mostly homogeneous DLC film was found in outside of the laser beam irradiated region, which was thinner on both edges of the film (near the shortest rims of the substrate, Fig. 9a). Such thickness dependence of the DLC film on both edges was caused by interactions between the flow dynamics of the reagent gas, the specific shape of the chamber and the plasma plume. These interactions resulted in a higher reagent gas ($H_2O_2$) concentration in regions, which "burned" more DLC film away from the substrate.

As the laser beam did not have completely homogeneous energy distribution on the substrate, different DLC film structures were created on the laser beam irradiated region (Fig. 9), which was a great opportunity to study differences in DLC film structures deposited during the same growth. Two different zones inside the laser beam irradiated region were observed. The DLC film was not grown (or it was grown only as a very thin and transparent film) inside of the intensive laser beam excitation zone. Inside the second zone, where the laser beam had lower intensity, non-homogeneous DLC films were grown (Fig. 9).

In figure 9 we can see the various DLC films, and the specific regions of films caused by the different reaction conditions.

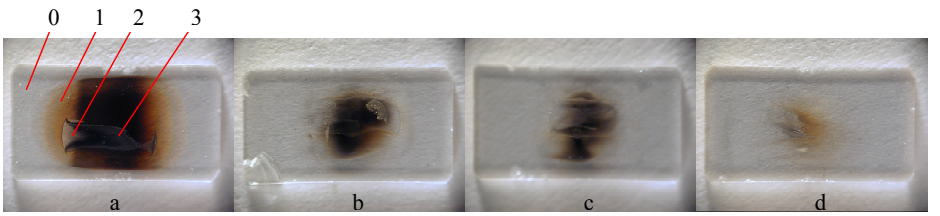


**Figure 9.** DLC films on the 1×8×15 mm fused silica substrates (0), where region No. 1 is DLC film outside the laser beam, region No. 2 was irradiated by the intense laser beam and there the DLC film did not grow or was grown very thin and transparent; and in region No. 3 non-homogeneous DLC films were grown at lower laser beam intensity. The films in figure 9 were deposited at different flow rates of the regent gas: (a) (film No. 4, table 1) was synthesized in the lowest gas flow, (b) and (c) (film No. 5 and 7, table 1) were synthesized in a medium gas flow and (d) (film No. 2, table 1) was synthesized in the highest gas flow from these films.

Optical inspection under higher magnification indicates that some of the films have interference-colored particles, which are situated on the edge of the laser beam irradiated region and are significantly different from the brown or grey areas located outside of the laser beam irradiated regions (Fig. 10). The colors of these particles are obviously due to the reflected light interference from the upper and lower surfaces. Therefore they must well transmit light up to ~3 eV, what means that the bandgap of this material must be even wider than $\Delta E > 3$ eV. The presence of these interference-colored particles indicates that there is a high content of $sp^3$ bonding carbon in this DLC film region.

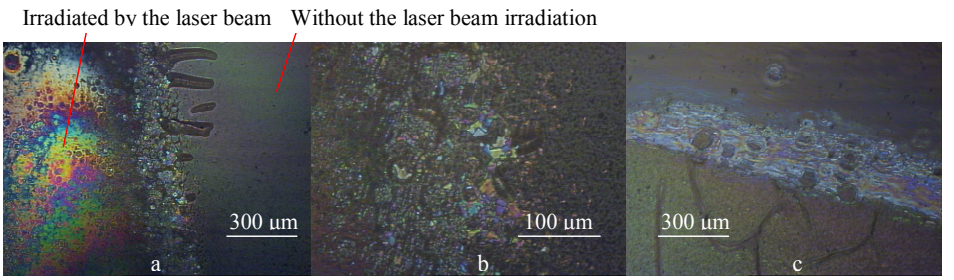


**Figure 10.** Interference colored particles on the laser beam irradiated regions where (a) is the DLC film No. 5 (table 1) with lateral dimensions of 1000×1300 µm, (b) is the same film with dimensions of 300×400 µm and (c) is DLC film No. 7 (table 1) with dimensions of 1000×1300 µm.

## 6.2. Raman spectroscopy data of the films

In figure 11, we compare the Raman spectra for DLC films, prepared in small PLD chamber (Figs. 4, and 5) under different deposition conditions (table 1). Spectra b, c and d have worse signal-to-noise ratios than other spectra because a photo-electron multiplier as a detector instead of the CCD camera was used. Figure 11a shows the Raman spectrum for DLC film No. 1 (table 1), which was measured for region outside of the laser beam irradiated opaque film region. There are two symmetrical lines in this spectrum with maxima at 1370 and 1600 $cm^{-1}$, which can be clearly identified as the D and G bands, respectively. The widths of these bands are ~200 $cm^{-1}$ and ~100 $cm^{-1}$, respectively. Comparing this spectrum with the spectrum provided in literature [42], we can conclude that this DLC film is disordered and has relatively high content of $sp^2$ hybridized, i.e. graphitized carbon. Figure 11b shows the Raman spectrum for DLC film No. 4 (table 1), measured for the laser beam irradiated bright zone. Spectrum in figure 11b can be fitted with two Gaussian curves, which results the D band maximum at 1409 $cm^{-1}$ and the G band maximum at 1547 $cm^{-1}$. Quite low frequency for the G band indicates a high content of $sp^3$ hybridized carbon in this DLC. This type of spectrum (G band situated at 1546 $cm^{-1}$) indicates that the $sp^3$ hybridized carbon content was about 85 % [41]. Figure 11c shows the

Raman spectrum for DLC film No. 4 (table 1), measured for opaque film zone, deposited outside of the laser beam irradiated region. This spectrum can also be fitted with two Gaussian curves having the D and G bands maxima at 1394 and 1572 $cm^{-1}$, respectively. Comparing this spectrum with the previous one, we can infer that there is much lower $sp^3$ hybridized carbon content in the film, because the maximum for G band occurs at higher wavenumber. Figure 11d shows the Raman spectrum for DLC film No. 3 (table 1), measured for the laser beam irradiated film region. This spectrum is relatively wide (bandwidth ~500 $cm^{-1}$) with a maximum located between 1350–1600 $cm^{-1}$. This is a second type of DLC spectrum, which has been presented more frequently than the spectra type given in figures 11b and 11c [66]. In this region of the film the estimated $sp^3$ hybridized carbon content is ~80 %. This estimate was attained based on the comparison of our spectrum with a literature data, where simultaneous Raman spectroscopy and electron energy loss spectroscopy measurements (EELS) were made [67]. Figure 11e shows the Raman spectrum for DLC film No. 7 (table 1), measured for the laser beam irradiated bright film zone. The spectrum has a wide (~400 $cm^{-1}$) band at ~1500 $cm^{-1}$ and this spectrum is very similar to the previous one, indicating that $sp^3$ hybridized carbon content is roughly the same [42, 43, 45, 66, 68, 69]. Figure 11f shows the Raman spectrum for DLC film No. 6 (table 1), measured for film area outside of the laser beam irradiated region. This spectrum can be fitted with three curves with maxima at ~1345, ~1480 and ~1580 $cm^{-1}$, respectively. Analysis of spectrum demonstrates that the distance between the D and G bands is quite small and it confirms the existence of disordered carbon structure in film (width of D and G band) [67]. Figure 11g shows the Raman spectrum for the same film No. 6 (table 1), but measured for the laser beam irradiated bright film zone. This spectrum can be fitted again using three curves, but the D and G bands have significantly smaller weight in the spectrum than it was established for the previous spectrum. The overall width of the spectrum is ~300 $cm^{-1}$ and maxima are located between 1350 and 1600 $cm^{-1}$. This spectrum is very similar to the spectra given in figures 11d and 11e, where the estimated $sp^3$ hybridized carbon content was relatively high.

Thus, for the laser beam irradiated region, the highest $sp^3$ hybridized carbon content was generally observed. For the regions located outside of the laser beam excitation region the content of $sp^3$ hybridized carbon was smaller, but could have been increased by increasing the $H_2O_2$ gas flow rate during film deposition.

Influence of the deposition parameters on the DLC film characteristics, deposited using synthesis setup No. 2 (Fig. 6) were observed using Raman scattering method. The main deposition parameters varied were: laser beam intensity, the amount (partial pressure) of $H_2O_2$ vapour in the deposition chamber and the substrate temperature.

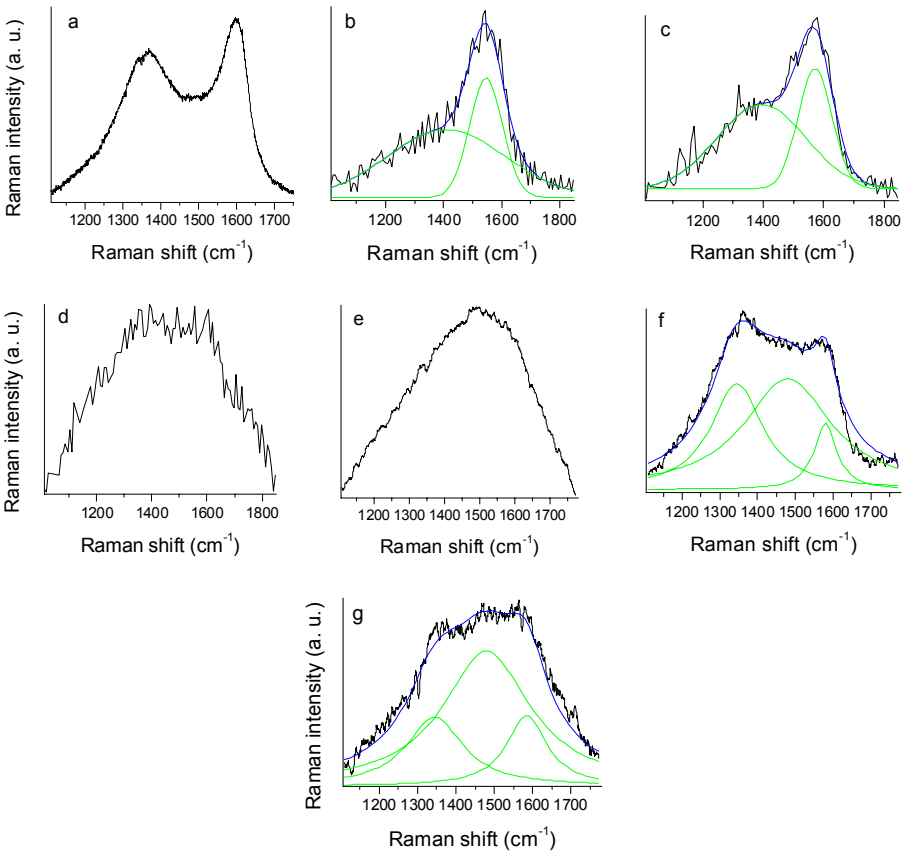


**Figure 11.** Raman spectra for the carbon films grown at different conditions (table 1), where: a) – film No. 1 (table 1), outside the laser beam irradiated opaque film region; b) – film No. 4 (table 1), inside the laser beam irradiated bright region; c) – film No. 4 (table 1), outside of the laser beam irradiated region; d) – film No. 3 (table 1), laser beam irradiated region; e) – film No. 7 (table 1), for laser beam irradiated bright area; f) – film No. 6 (table 1), outside of the laser beam irradiated region; g) – film No. 6 (table 1), for laser beam irradiated bright zone.

It was found that the main influence of laser beam intensity appeared to the G band position in the Raman spectra. It is probable that when the laser beam intensity is increased, it can induce bigger $sp^2$-hybridized carbon clusters deformation and partial transformation to the $sp^3$-hybridization state. Such transformation is generally accompanied by a shift of G band towards shorter wavenumbers as can be seen in figure 12.

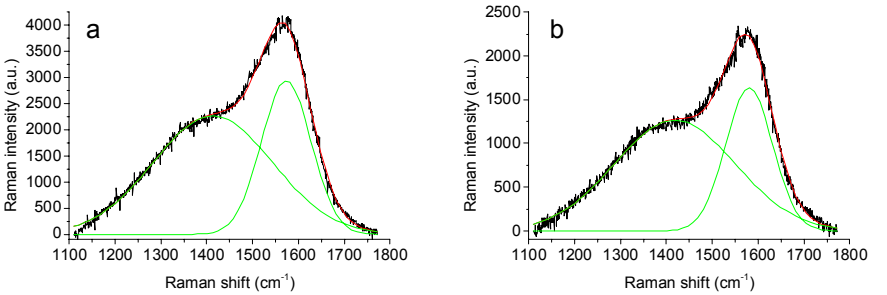


**Figure 12.** Raman spectra for the DLC films, deposited using 35 mJ (a) and 25 mJ (b) laser beam intensity. Both films were deposited at 500°C substrate temperature using 3000 laser pulse in $9x10^{-3}$ mbar $H_2O_2$ vapor pressure. Both films were deposited using additional film excitation by the laser beam.

Raman spectra in figure 12 characterise DLC films with only difference in deposition conditions being the laser beam intensity. Laser beam intensity is the main reason why G band for DLC film shifts from 1573 $cm^{-1}$ (a) to the 1580 $cm^{-1}$ (b) in the Raman spectra under discussion.

The influence of $H_2O_2$ vapour on the DLC films structure was estimated using the Raman spectra given in figure 13, where the $H_2O_2$ vapour concentration was varied during the deposition process.

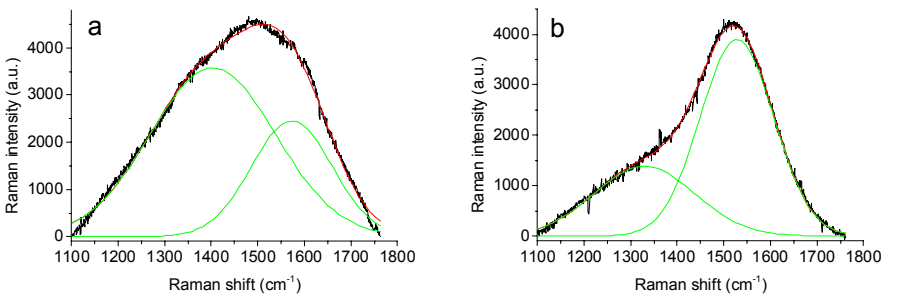


**Figure 13.** Raman spectra of the DLC films deposited in 1.9 mbar (a) and $2.7x10^{-3}$ mbar $H_2O_2$ vapor pressure. (b) Both films were deposited at 22°C substrate temperature using 5000 laser pulse with 130 mJ energy (without additional laser activation of surface layer).

In figure 13a we can see that the ratio of Raman intensities $I_D/I_G$ (2.26) is much higher than in figure 13b (0.48). The increase of the D band intensity as compared with the G band intensity and its shift to the higher frequencies means, that in this film the number of ordered aromatic carbon rings increases with decreasing the size of aromatic clusters [46]. Very similar Raman spectra

were published in literature [42, 43, 45, 66, 69, 70], where ~80% $sp^3$-hybridized carbon content was calculated, based on the EELS data [67].

At higher substrate temperatures D band in Raman spectra increases and shifts together with the G band toward the higher frequencies, as demonstrated in figure 14. In this figure we can see two different shapes of Raman spectra for DLC films deposited at different conditions. DLC film structure depends mainly on the substrate temperature and the number of laser pulses does not have an important influence on the film structure (it changes mainly the film thickness).

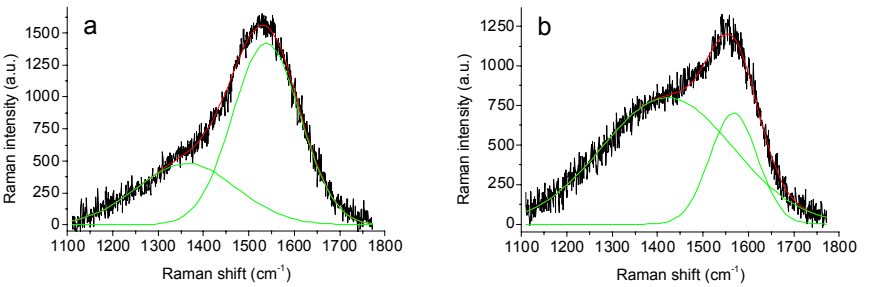


**Figure 14.** Raman spectra for the DLC films deposited at 100°C (a) and 600°C (b) substrate temperature. Both films were deposited using 35 mJ laser beam intensity and $9x10^{-3}$ mbar $H_2O_2$ vapor pressure. During deposition, the films surfaces were additionally irradiated by the laser beam. Number of laser pulses for (a) and (b) were 3000 and 2000, respectively.

The increase of D band intensity and its shift to the higher frequencies is related with the increase of clusters of $sp^2$ sites in six fold aromatic rings [45–47]. Observed G band shift to higher wavenumbers (1538 $cm^{-1}$ → 1567 $cm^{-1}$) at higher substrate temperatures can be explained by the excitation of carbon particles on the substrate surface to surpass the activation energy barrier between the $sp^3$-and $sp^2$-hybridized carbon state. Such equilibrium promotes preferably a lower energetic state, which in this case is graphitic structure. Graphitic structure is characterized by shorter bonds (on sheet) compared to average DLC bonds, and therefore bigger oscillation frequencies, which appear in G band shifting to the higher wavenumbers in Raman spectra.

Using the Raman spectra for several DLC films, grown at different substrate temperatures, a linear dependence between the substrate temperature and G band scattering maximum position was observed, given in figure 15.

As the G band is shifting to the higher frequency at higher deposition temperature (Fig. 15), we conclude that carbon films graphitization take place at high growth temperatures.

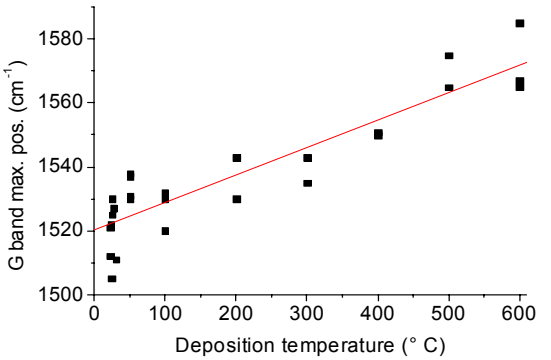


**Figure 15.** DLC films Raman spectra G band maximum position dependence on substrate temperature.

Among of the many a-C Raman scattering spectra measured for carbon layers prepared by setup No. 3 (Fig. 7), some spectra contained narrow diamond peaks (Fig. 16). All these films were deposited under laser irradiation condition (pulse energy 20 mJ), were observed.

It was established, that in the Raman spectra a diamond peak appeared only for these carbon films, which substrates were irradiated by the laser pulses having energy near ~20 mJ. For several other carbon films, deposited only at slightly different irradiated laser beam intensities (from 4 to 16 and from 22 to 100 mJ), that kind of diamond peak has not been observed. It should be noted, that our irradiated laser beam (flat cross-section surface area ~5×12 mm) guided onto the growing film does not have an absolutely homogeneous energy distribution. Thus, at the time being we can not give the very exact energy values per unit substrate area. Initiated by applied laser beam nonhomogeneity, deposited carbon film surfaces were inhomogeneous as well (Fig. 16), established by different shape of Raman spectrum. We can see in figure 16, that pure diamond peak intensity is very strongly variable for these films, and this indicated again that the suitable intensity "window" of the irradiating beam is very narrow (at ~20 mJ for our deposition system). The appearing diamond peak maximum is situated in the region from 1330 $cm^{-1}$ to 1335 $cm^{-1}$ in the Raman spectrum.

Very distinctive diamond peaks presented in Raman spectra, given in figure 16c and 16d, were fitted by Lorentzian curves. Good fittings for other a-C regions were achieved using two Gaussian curves (Fig. 16a and 16b). Appearing diamond peak shape and frequency of Raman peaks for a-C films deposited indicates that diamond structure is presented as an individual phase in a-C, but not as an integrated material with other carbon allotropic forms, like it was observed for many DLC films discussed in literature [42, 43, 71].

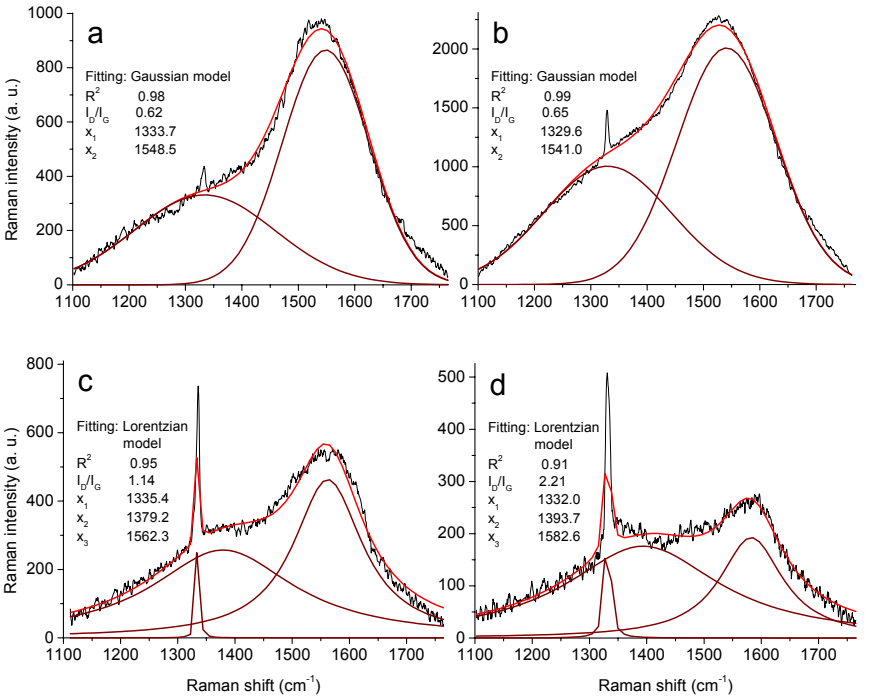


**Figure 16.** Raman spectra of the amorphous carbon (a-C) film regions, deposited at room temperature, ~$10^{-3}$ mbar pressure, interval deposition. Between three ablation pulses (frequency 5 Hz and 100 mJ energy per pulse), the substrate has been irradiated by one laser pulse (20 mJ energy per pulse) and total 1000 cycles has been used. (A) to (c) are listed by the applied irradiated laser beam local intensity increasing (different film regions on substrate).

However, from these Raman spectra it can be concluded that diamond phase formation is seemingly related with the graphitization process (G band shifts toward the higher frequencies) and in many cases even competes with it. It is possible that carbon graphitization processes occur at only slightly different conditions next to the $sp^3$ hybridization state carbon formation promotion. Systematic analysis of D band evolution and the ratio of integral intensities for D and G bands $I_D/I_G$ in Raman spectra (data listed in Fig. 16–18) for amorphous carbon films indicates, that substrate laser beam irradiation promote the $sp^2$ sites six fold aromatic rings formation due to D band intensity increase [45].

Figure 17 presents the Raman spectrum of an a-C film, which deposition cycle consisted of 3 ablation pulses (5 Hz and 100 mJ energy per pulse) followed by the film irradiation by 10 laser pulses (100 mJ energy per pulse and frequency f=25 Hz). For the film deposition the total number of cycles was 1000. Raman spectrum for a-C film, deposited without substrate excitation, is given in figure 18. Comparison of these data with those given in figures 16 to 17 demonstrates that the laser beam irradiation have a noticeable influence on the G band position

in Raman spectra. At lower laser beam irradiation intensity, the G band shifts toward the lower frequency and with increasing the laser beam intensity it shifts again to the higher frequency values. G band shift toward lower frequency is correlated with the increasing content of carbon in $sp^3$ hybridization state in the DLC film [46]. Comparison of Raman spectra for a-C films, given in figures 16 to 18, demonstrates that $sp^3$ hybridized carbon graphitization takes place preferable at higher energy intensities (>20 mJ) of substrate using laser irradiation. Similar kind of DLC film graphitization by irradiating laser beam was performed and analyzed by Yasumaru [72]. It can be supposed from Raman spectra analysis, that the laser beam irradiation promotes the DLC structure formation, but at higher intensities, it causes the graphitization of DLC structure. Individual diamond phase formation takes place under laser beam irradiation conditions, occurring even when the background DLC film partly graphitizes under the influence of laser irradiation (Fig. 16).

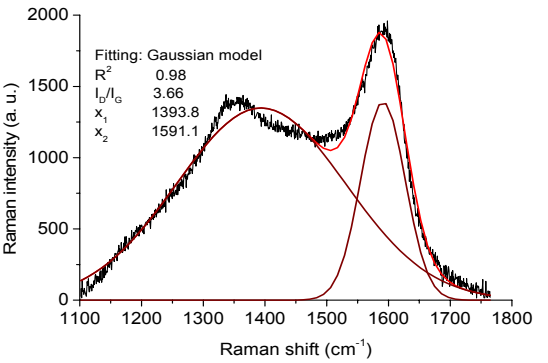


**Figure 17.** Raman spectrum for the a-C film, deposited at room temperature, ~$10^{-3}$ mbar pressure. During the growth, 3 ablation pulses (5 Hz and 100 mJ energy per pulse) were followed by 10 surface excitation pulses (25 Hz and 100 mJ energy per pulse). Total number of cycles was 1000.

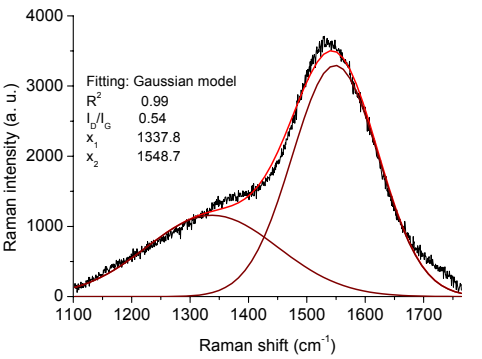


**Figure 18.** Raman spectrum for the a-C film, deposited at room temperature, ~$10^{-3}$ mbar pressure, using 20000 laser pulses (5 Hz and 100 mJ energy per pulse).

Raman spectrum (Fig. 19) for carbon films, which were synthesised for electrochemical applications, consist of two broad bands peaking at 1353 $cm^{-1}$ (D band with the integral intensity $I_D$) and at 1541 $cm^{-1}$ (G band with the integral intensity $I_G$). The ratio of the integral intensities of these two bands is $I_D/I_G$=0.75, and the widths of the spectral bands are 264 $cm^{-1}$ and 160 $cm^{-1}$, respectively. Comparison of our results with the literature data [20, 23, 41, 66] shows that the shape of the spectrum in figure 19 is typical for amorphous DLC films with a relatively high content of carbon in the $sp^3$ hybridization state. Based on results of works [41, 66], where the Raman spectra and electron energy loss spectra (EELS) were correlated for samples with different contents of carbon in the $sp^3$ hybridization state, it is possible to calculate that the ratio of carbon in $sp^3/sp^2$ hybridization states is >0.8. However, taking into account the fact that the G band is shifted toward smaller wave numbers (1541 $cm^{-1}$) compared with pure graphite (1580 $cm^{-1}$), the ratio of the $sp^3/sp^2$ hybridization states is probably somewhat higher than 0.8. This conclusion is in agreement with results [39, 40], where the shift of the G band toward higher wave numbers has been explained by a higher content of carbon in the $sp^2$ valence state in DLCE samples.

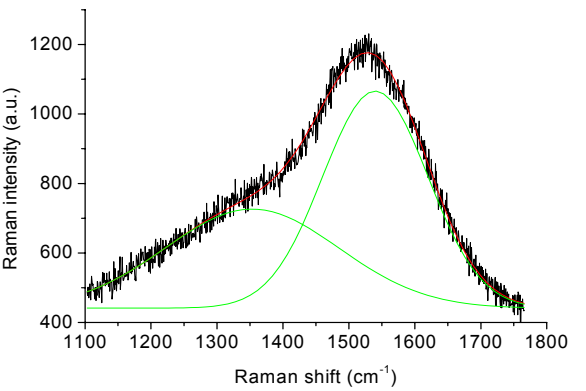


**Figure 19.** Raman spectrum of a DLC film deposited on a carbon substrate.

## 6.3. Atomic force microscopy data of the films

The main representing parameter characterizing the surface morphology is a root-mean-square (RMS) roughness:

$$\mathrm{RMS} = \sqrt{\frac{\sum_{n=1}^{N} \left(Z_n - \overline{Z}\right)^2}{N - 1}},$$

$N$ is a number of data points and $\overline{Z}$ is an average height.

The AFM measurements of DLC films, which were prepared in extremely small vacuum chamber, indicated that the laser beam irradiated regions have smoother surfaces, than those deposited outside of the laser beam irradiated surface region. For example, the film No. 6 (table 1) has RMS ~370 Å on the laser beam irradiated region, but over 420 Å outside of the laser beam irradiated area. Especially smooth surfaces were observed for the colored particles, deposited inside the laser beam irradiated zones. Thus, for example for film No 5 (table 1), the RMS is ~50 Å on the colored particle but alongside the colored particles (also in the laser beam irradiated zone) the RMS is ~100 Å. In figure 20, two AFM images for the film No. 5 (table 1) are presented. These images were recorded for the colored particle surface in the laser beam irradiated zone (Fig. 20a), and alongside the colored particles in the laser beam irradiated zone (Fig. 20b).

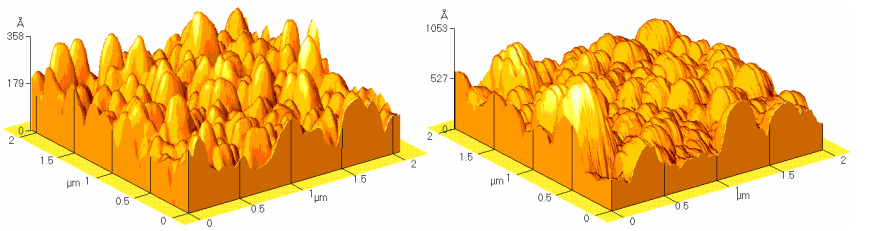


a b

**Figure 20.** AFM 3D images (contact regime) of the DLC film No. 5 (table 1) surface, where (a) was recorded from a colored particle in the laser beam irradiated zone and (b) was recorded alongside the colored particles also in the laser beam irradiated zone.

From the AFM studies it was found that on the film surfaces the sizes of most particles range from 10 to 400 nm. Knowing the sizes of particles, it is possible to make conclusions about the origin of D band in the Raman spectra. In principle, it is possible that the appearance of the D band is due to the fine size graphite particles presented in the films. Between the integral intensities of D and G bands ($I_D/I_G$) and the size of the graphite crystallites ($L$), the following empirical relation exists: $L = 44\frac{I_G}{I_D}$ (Å) [39].

If L = 100 – 4000 Å then $I_D/I_G$ = 0.44 – 0.01. For all the spectra depicted in figure 11, the $I_D/I_G$ ratio is bigger than 0.44, and hence these particles cannot represent fine size graphite particles.

AFM results indicate that the most influencing parameter in the deposition process was the substrate temperature. In figure 21, the dependences of RMS roughness on the growth substrate temperature are given (other deposition parameters were similar).

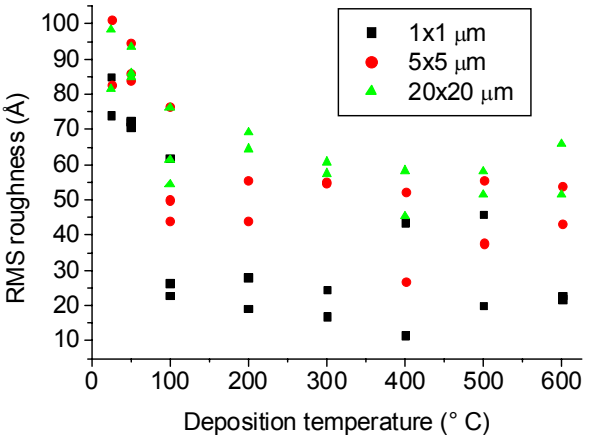


**Figure 21.** DLC films RMS roughness dependences from substrate temperature on the 1×1 μm, 5×5 μm and 20×20 μm films areas.

According to these data it was established that noticeable RMS roughness change occurs at temperatures between from 50 to 100°C. At higher temperatures the RMS roughness values approach to the plateau. 3D images for DLC films deposited at different temperatures can be seen in figure 22. Two upper AFM images in figure 22 characterize DLC film structure deposited at 25°C substrate temperature, (40 mJ laser beam intensity, $9.7\times10^{-3}$ mbar $H_2O_2$ vapor pressure and 3500 laser pulses, setup No. 2, Fig. 6). Two lower AFM images were made from DLC films, which were deposited at 400°C substrate temperature, (35 mJ laser beam intensity, $9.5\times10^{-3}$ mbar $H_2O_2$ vapor pressure and 3000 laser pulses, setup No. 2, Fig. 6). In both experiments the additional laser beam excitation method was used.

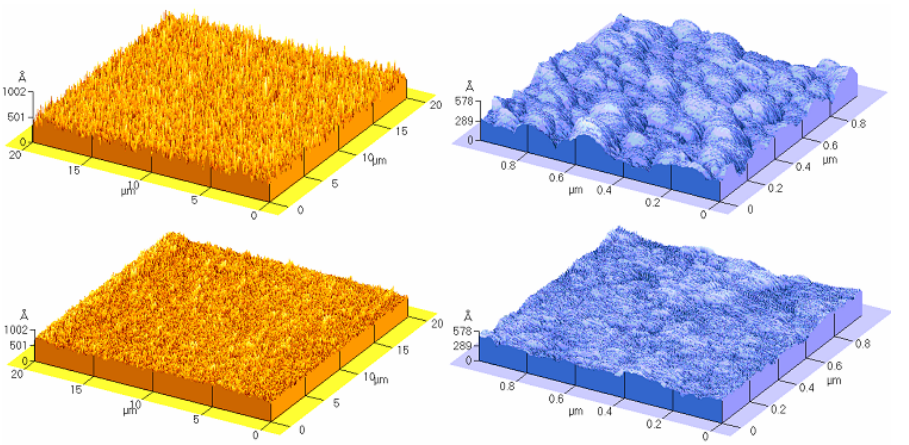

**Figure 22.** AFM 3D images (contact regime) for DLC films (upper areas were deposited at 25°C and lower areas were deposited at 400°C).

Figure 22 demonstrates that at lower deposition temperature, the bigger grain size: 50–150 nm, and smoother surface profile at higher deposition temperatures were observed. The RMS roughness of these films is 74 Å and 44 Å (for 1×1 μm surface area) and 82 Å and 58 Å (for 20×20 μm surface area), respectively.

According to the literature data on the RMS roughness values for DLCs, discrepant tendencies are discussed regarding the influence of the deposition temperature. It should be noted that based on the results of Ref. [73], a noticeable cluster formation at higher deposition temperatures is possible. This may lead to drastically increased RMS values if using the AFM data measured from the bigger surface areas as compared to the size of clusters.

AFM data for DLC films, prepared by setup No. 3 (Fig. 6) and given in figure 23 show that the films containing more diamond crystals (based on the Raman spectroscopy data, i.e., areas of films corresponding to figures 16c and d) demonstrate noticeable phase segregation for deposited films (Fig. 23a and b), differently from the surfaces, prepared at higher or lower (Fig. 23c and d) additional laser surface treatment intensities applied. At optional diamond phase formation conditions (20 mJ energy per pulse) the very big (220×250 nm, sometimes even 2×1 μm) and comparatively flat homogeneous diamond crystals have been deposited. However, relatively high root mean square surface roughness values, RMS

≥ 144 nm, have been calculated due to the high macroscopic inhomogeneity of more diamond crystals containing deposits. The RMS values for more amorphous carbon (graphite like) films are noticeably lower, RMS ≤ 8.7 nm, and the films under study have more homogenous amorphous surface structure (Fig. 23c and d).

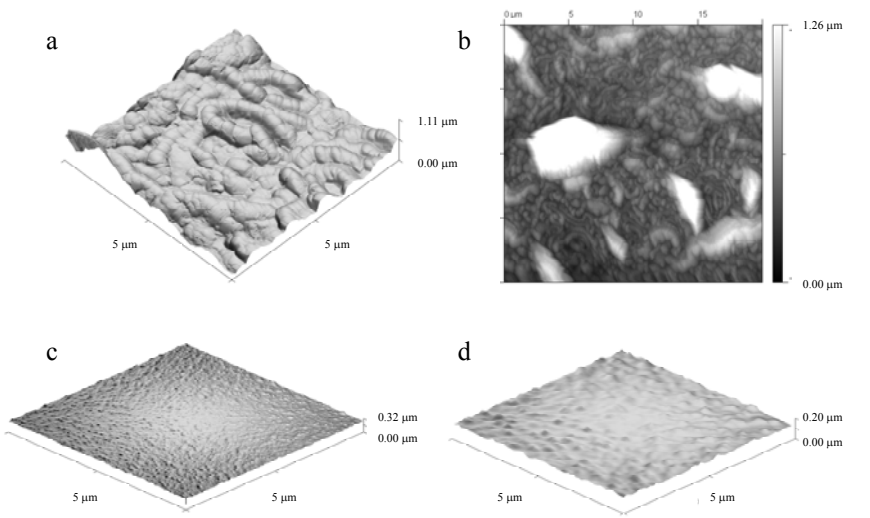


**Figure 23.** AFM 3D and 2D images (noncontact regime) for DLC film areas 5×5 μm (a), 20×20 μm (b) for the similar areas like it was used for the Raman spectroscopy analysis given in figure 16c-d (i.e. for more diamond crystals containing areas of carbon films) and 5×5 μm (c), 2×2 μm (d) for the similar areas like it was studied in figure 16a (i.e. for more graphitized deposits).

Thus, it was found that formation of the comparatively large diamond crystals inside of the carbon film deposited is possible under very well controlled additional surface irradiation conditions.

AFM images of the carbon substrate (CY-2500) surface and DLCE coatings were also measured in contact-mode regime and the results are shown in figure 24. The RMS values of these surfaces (determined from 1×1 μm DLCE areas) were 41 Å and 68 Å, respectively. Consequently, the roughness of DLC films is higher as compared with the initial surfaces of the glossy carbon substrate, and DLC particles have an average size of about 0.1 μm.

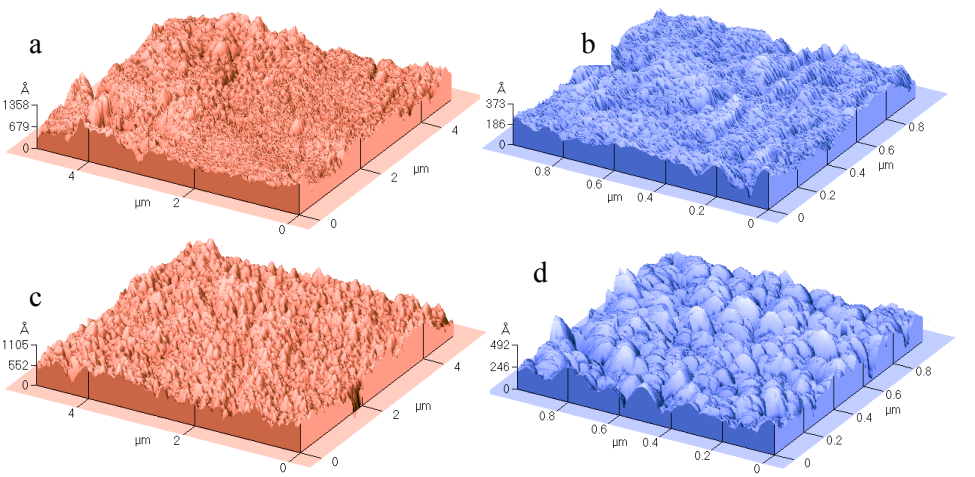


**Figure 24.** AFM images (contact regime) of carbon substrates (a and b) and DLC films grown on the same substrates(c and d). The image areas are 5×5 μm (a, c) or 1×1 μm (b, d).

## 6.4. Cyclic voltammograms (CV)

The CVs shown in figure 25a indicate that in the potential region $-0.4 < E < 1.0$ V [vs. AgCl|Ag (sat. KCl in $H_2O$)] the current density values are low and depend slightly on the potential scan rate and, thus, in this potential region there are no rapid faradaic processes at the DLCE|0.1 M NaF aqueous solution interface. At $E < -0.4$ V, a rapid reduction process begins at the DLCE|0.1 M NaF aqueous solution interface.

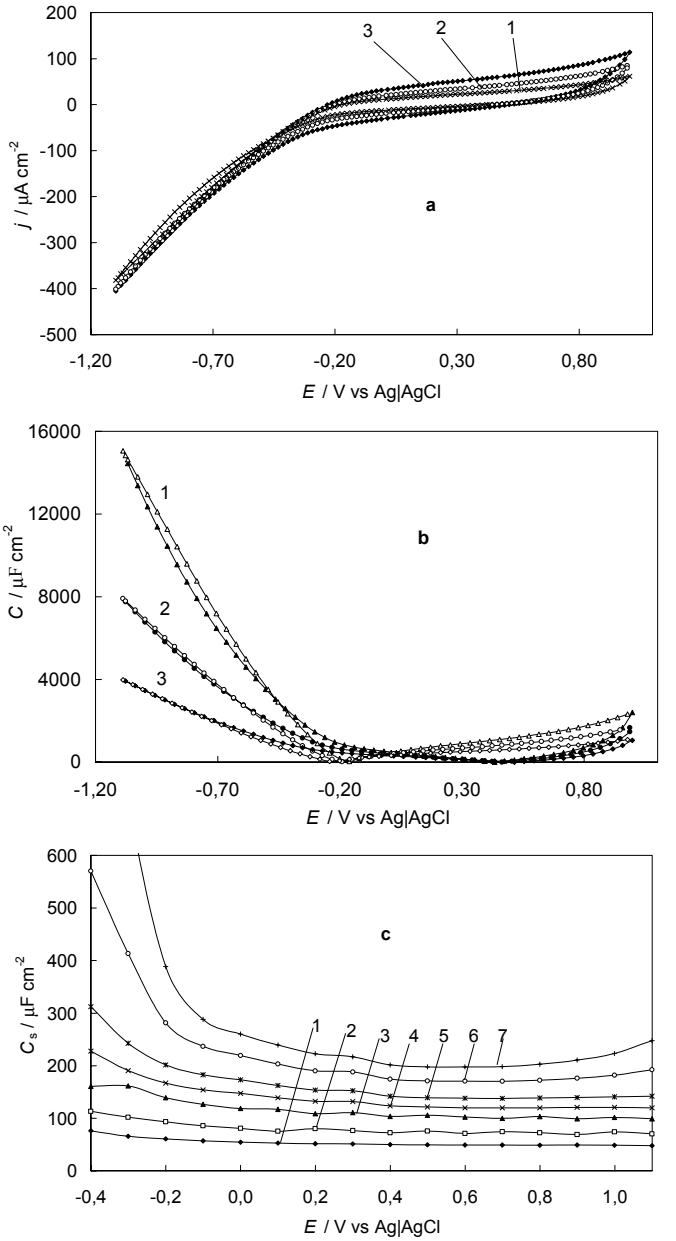


**Figure 25.** (a) Current density vs. electrode potential curves and (b) differential capacitance vs. electrode potential curves (calculated from *j* vs. *E* curves; *open symbols*: potential scan toward less negative potentials; *filled symbols*: potential scan toward more negative potentials) for the DLCE in 0.001 M NaF solution at different potential scan rates (mV s-1): 25 (*1*), 50 (*2*) and 100 (*3*). (c) Differential series capacitance $C_S$ vs. *E* curves obtained from *Z``* vs. *Z`* curves at different a.c. frequencies (Hz): 10 (*1*), 5.2 (*2*), 2.0 (*3*), 1.0 (*4*), 0.52 (*5*), 0.19 (*6*) and 0.10 (*7*)

The shape of the $j$ vs. $E$ curves is typical of carbon electrodes in the region –0.4 < $E$ < 1.0 V [5, 6, 9] and the capacitance values, $C$ (Fig. 25b), calculated from $j$ vs. $E$ plots ($C=j/v$, where $v=dE/dt$ is the electrode potential scan rate), are in reasonable agreement with the series capacitance values ($C_S$) obtained from the impedance complex plane plots at a frequency $v\approx0.1$ Hz (Fig. 25c) (-$Z$`` vs. $Z$`, i.e. so-called Nyquist plots [74–85]: $Z``=(jC_S2\pi v)^{-1}$; $j=\sqrt{-1}$). The values of $C$ are practically independent of $v$ in the potential region from –0.30 to 0.80 V. Thus, this potential region corresponds to the region of nearly ideal polarizability of DLCEs [74–89]. At $E$ < –0.40 V, the capacitance values decrease with the increase of the potential scan rate (Fig. 25b) and this effect can be explained by the very high resistance values (i.e. by the very high potential drop [5, 6]) inside the carbon electrode material [90–92]). It should be noted that additional studies in less concentrated electrolyte solutions are required to give more detailed analysis of results.

## 6.5. Impedance complex plane plots

The impedance complex plane plots obtained at various fixed electrode potentials ($E$=const.; –0.4 < $E$ < 1.1 V) and at different NaF concentrations, presented in figures 26a, 27a and 28a, indicate that the shape of the $Z``$ vs. $Z`$ plots depends noticeably on $E$, i.e. on the surface charge density, $\sigma$, of the DLCE. At potentials –0.4 < E < 1.2 V [vs. AgCl|Ag (sat. KCl in $H_2O$)], a depressed semicircle in the high-frequency region and nearly so-called mixed kinetic mass transfer and "capacitive" behaviour (i.e. finite length effects [5, 6, 84–89]) in the low-frequency region ($v$ < 10 Hz) are observed. Differently from the nanoporous carbon electrodes, there is no so-called micro-porous region in $Z``$ vs. $Z`$ plots with a slope of 45° in the region of moderate frequencies [5, 6, 57, 58, 75–85]. It can be seen that, the curvature of the $Z``$ vs. $Z`$ plots increases noticeably with the negative surface charge density, but the width of the depressed semicircle observed at higher frequency ($v$ > 19 Hz) is practically independent of $E$. Comparison of the results in figures 26a, 27a and 28a shows that, at higher frequencies, the width of the first semicircle, i.e. the total series resistance (probably the sum of charge transfer and the bulk electrolyte resistance), increases with the dilution of the electrolyte solution.

The influence of the partial charge transfer process increases with the negative polarization (Figs. 26a, 27a and 28a), and at $E \le$ –0.4 V [vs. Ag|AgCl (sat. KCl)] there are two depressed semicircles in the complex plane plot, which can be explained by the increase of influence of the parallel charge transfer process, i.e. by the decrease in resistance with the increase of electrochemical process rate of the cathodic faradaic processes (probably reduction of surface-active functional groups, reduction of $H^+$ or adsorption of $Na^+$ following a partial charge transfer process to the DLCE from the $Na^+$ ions during the Gibbs adsorption step [5, 6]) at the negatively charged surface of the DLCE.

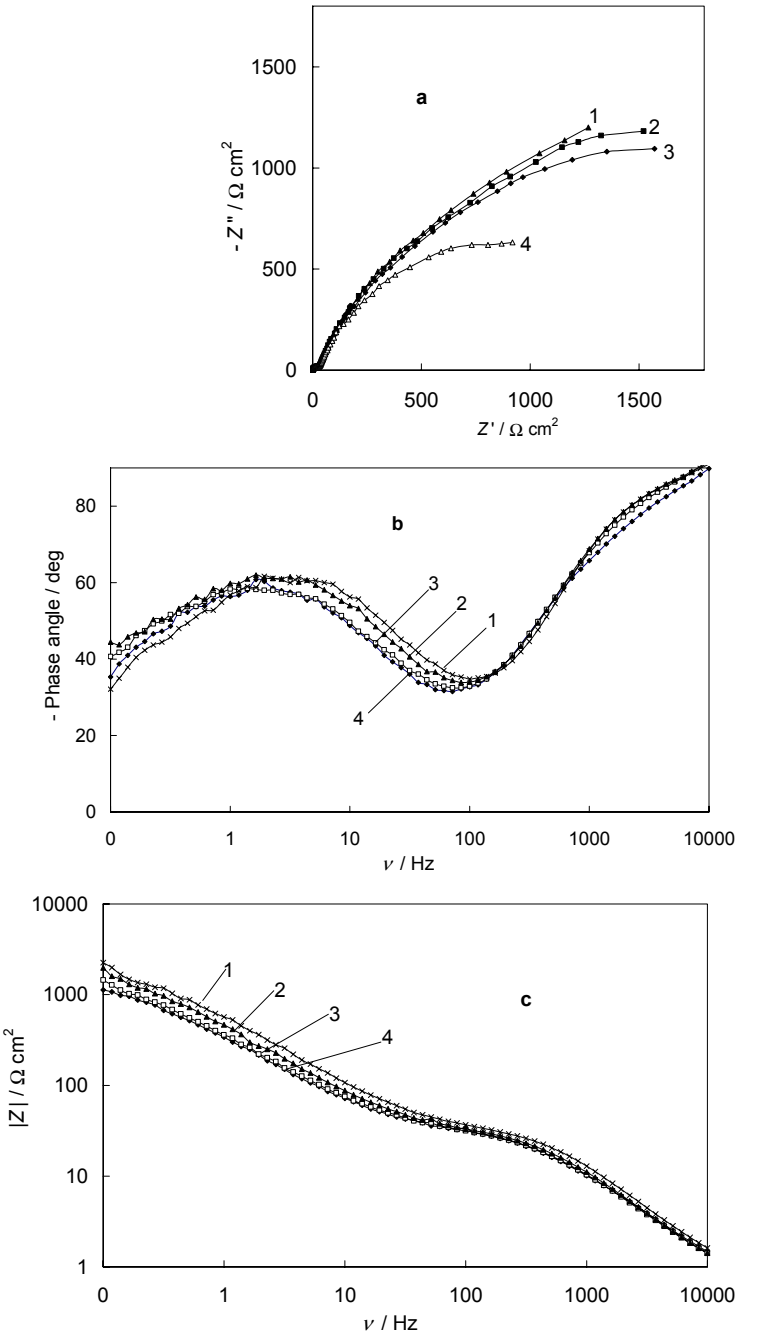


**Figure 26.** (a) Complex plane plots [at electrode potentials (V): 0.2 (*1*), 0.6 (*2*), 1.1 (*3*) and –0.4 (*4*)]; (b) phase angle vs. a.c. frequency plots and (c) complex impedance vs. a.c. frequency plots [at electrode potentials (V): 1.1 (*1*), 0.2 (*2*), –0.2 (*3*) and –0.4 (*4*)] for the DLCE|0.1 M NaF+$H_2O$ interface. Potentials have been given vs. Ag|AgCl (sat. KCl in $H_2O$) in all figures.

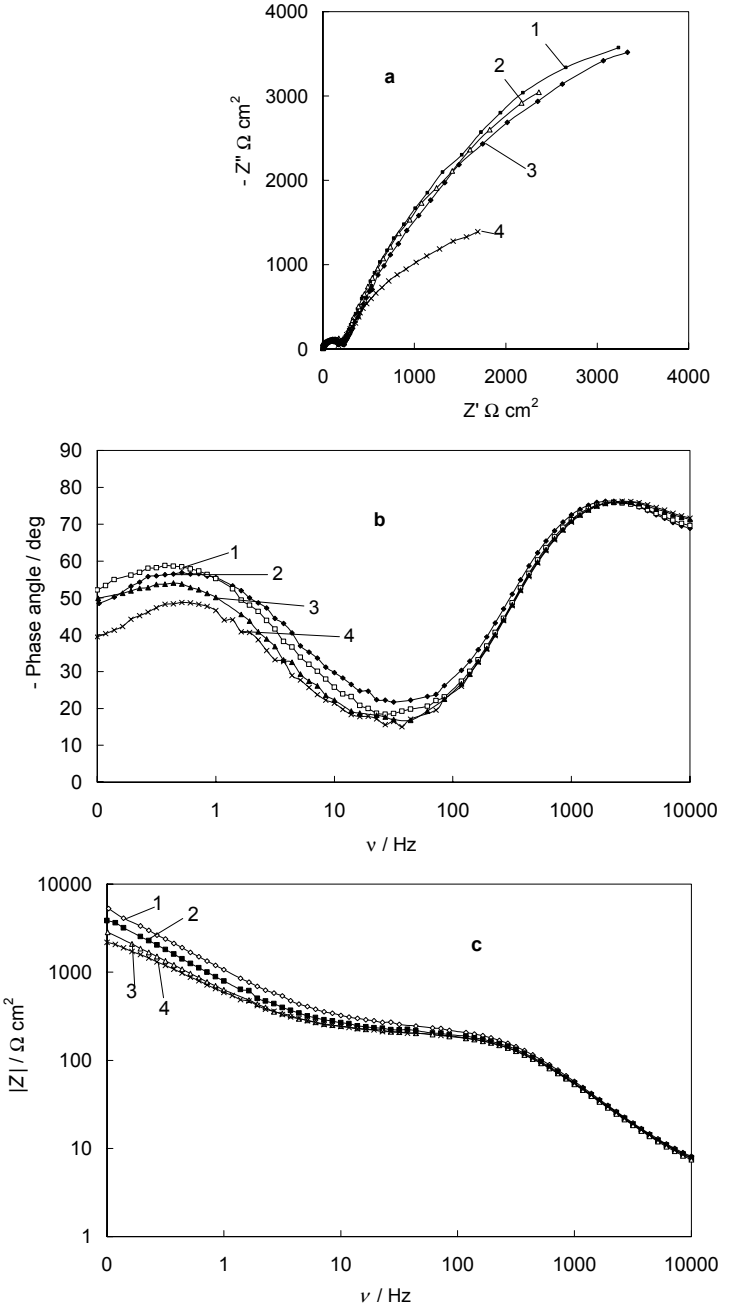


**Figure 27.** (a) Complex plane plots [given at electrode potentials (V): 0.6 (*1*), 0.2 (*2*), 1.1 (*3*) and –0.4 (*4*)]; (b) phase angle vs. a.c. frequency plots and (c) complex impedance vs. a.c. frequency plots [at electrode potentials (V): 1.1 (*1*), 0.2 (*2*), –0.2 (*3*) and –0.4 (*4*)] for the DLCE|0.01 M NaF+$H_2O$ interface.

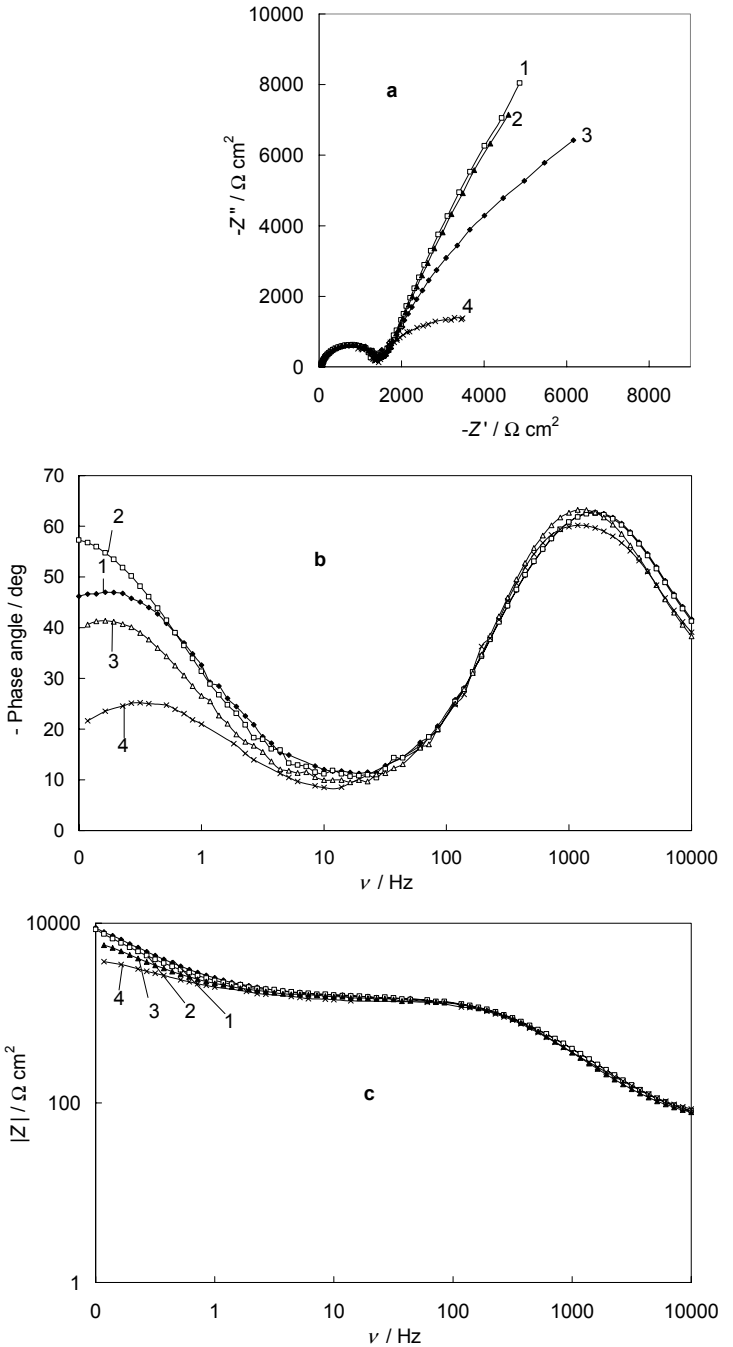


**Figure 28.** (a) Complex plane plots [at electrode potentials (V): 0.6 (*1*), 0.2 (*2*), 1.1 (*3*) and –0.4 (*4*)]; (b) phase angle vs. a.c. frequency plots and (c) complex impedance vs. a.c. frequency plots [at electrode potentials (V): 1.1 (*1*), 0.2 (*2*), –0.2 (*3*) and –0.4 (*4*)] for the DLCE| 0.001 M NaF+$H_2O$ interface.

Analysis of complex plane plots shows that the frequency for the maximum of the depressed semicircle in the high-frequency region of the $Z``$ vs. $Z`$ plots is practically independent of the electrolyte concentration as well as of the electrode potential studied (if $E \geq -0.3$ V). Thus, the frequency $\omega_{max}=(\tau_{max})^{-1} = (R_bC_b)^{-1}$ (where $\tau_{max}$ is the characteristic relaxation time and $R_b$ and $C_b$ are the total resistance and total capacitance of the bulk electrolyte and electrode material, i.e. the capacitance of a "flat" electrode and the resistance of the high-frequency processes occurring on it) seems to be characteristic of the surface of the solid material|electric double layer interface. It is probably caused mainly by the space charge effects in the surface layer of the carbon material [76–78] and by the macroscopic Helmholtz layer capacitance characteristics for the flat electrode as well as by the diffuse (Gouy) layer characteristics. The value of $R_b$ can be obtained from the Nyquist ($Z``$ vs. $Z`$) plot, where the low-frequency and the high-frequency ends of the straight line coincide with series resistance Rs value [5, 6, 74–85]. The frequency of the inflection point between the semicircle and the so-called capacitive (in our case nearly capacitive) region of the $Z``$ vs. $Z`$ plots at $\nu < 10$ Hz is practically independent of $c_{NaF}$ as well as of $E$, and probably characterizes the interplay of a.c. penetration depth $\lambda$ and the macroscopic surface roughness characteristics of the DLCE [5, 6].

The Bode plots (i.e. the phase angle $|\delta|$ and complex impedance $|Z|$ vs. log dependences) (Figs. 26, 27, 28, parts (b) and (c)) indicate that there is a minimum in the $|\delta|$ vs. log curves ($|\delta| < 10$ for $1\times10^{-3}$ M NaF) and, thus, there are no processes (faradaic) on the DLCE|NaF+$H_2O$ interface with characteristic frequency values in this region of $\nu$. At fixed electrolyte concentrations the values of $|Z|$ and $|\delta|$ do not depend on the potential if $\nu \geq 100$ Hz. For 0.01 M and 0.001 M electrolyte solutions, there is a maximum in the $|\delta|$ vs. log$\nu$ curves with the value $|\delta| \geq 63°$, characteristic of the kinetically mixed process ($\delta = -45°$ for diffusion limitation and $\delta \approx -90°$ for pure capacitive behaviour [5, 6]). The absolute value of the phase angle $\delta$ and the frequency maximum increase with the electrolyte concentration. Thus, deviation of the DLCE|$x$M NaF+$H_2O$ interface from the behaviour characteristic of the pure capacitive behaviors increases with dilution of the electrolyte.

At smaller frequencies (Figs. 26, 27, 28, parts (b) and (c)), the values of $|Z|$ and $|\delta|$ start to increase, and at $0.05 \leq \nu \leq 10$ Hz there is a maximum in the $\delta$ vs. log$\nu$ plot with the value $\delta \geq 65°$ (for $1\times10^{-1}$ M), which is mainly characteristic of the kinetically mixed limited process at the rough surfaces (adsorption and diffusion-limited stages in the interior of the electrolyte). The slope of the $|\delta|$ vs. log$\nu$ dependence remarkably depends on cNaF and the maximum values of $|\delta| \geq 45°$ for $c_{NaF} = 0.001$ M have been established only at very low frequencies ($\nu \leq 0.1$ Hz). This result is probably caused mainly by the interplay of the Debye screening length and surface roughness of the DLCE electrode [6, 63–65, 93, 94]. With the increase of the electrolyte concentration, the frequency of this frequency maximum, $\nu_{max}^{If}$ (in the low-frequency region), shifts toward

higher frequencies, i.e. toward smaller relaxation times $\left(\tau_{\max}^{If} = (\nu_{\max}^{If})^{-1}\right)$. The values of $|\delta|$ are maximal at E≈0.2 V and the dependence of $|\delta|$ on $c_{NaF}$ is more noticeable for more dilute solutions ($c_{NaF} \le 1\times10^{-3}$ M).

In comparison with a nanoporous carbon electrode (NPCE), the low-frequency characteristic relaxation time, $\tau_{\max}^{If}$, is noticeably shorter for a DLCE than for a NPCE (approximately $10^3$ times) [6]. The dependence of the series capacitance $C_S$ [obtained from $Z` = (j2\pi\nu C_S)^{-1}$] and parallel capacitance $C_P$ on $\omega^{1/2}$ (Fig. 29a) and $C_S$, $C_P$ and $R_P$ on log$\nu$ are in a good agreement with the conclusion made above, and the coincidence of these dependences in the region $10 < \nu < 10{,}000$ Hz (Fig. 29b and c) indicates that there is no rapid faradaic charge transfer reactions at the DLCE|$x$M NaF+$H_2O$ interface. The series capacitance values $C_S$ decrease on dilution of the electrolyte; thus, weak adsorption of $Na^+$ cations on the DLCE is possible.

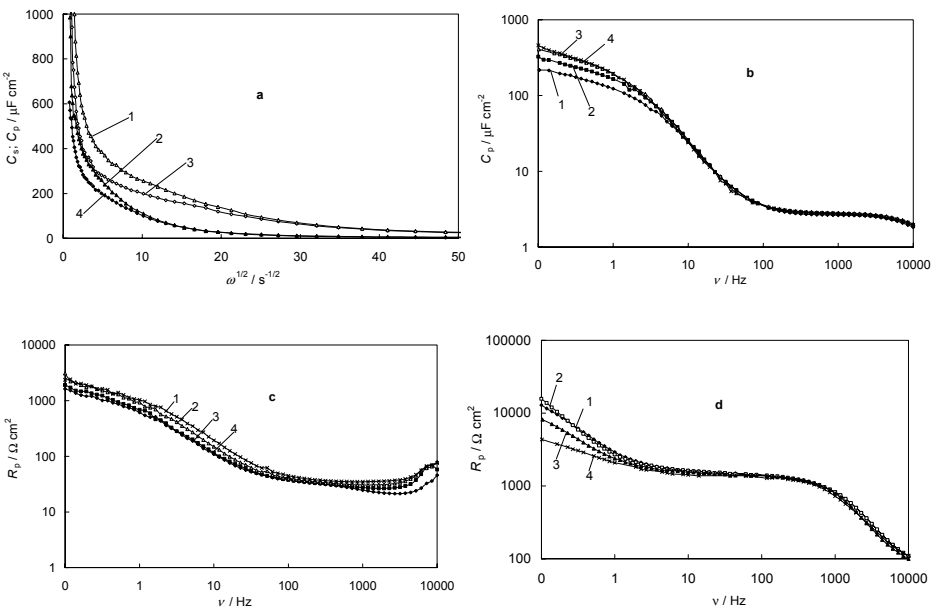


**Figure 29.** (a) Dependence of $C_S$ (*1, 3*) and $C_P$ (*2, 4*) on $\omega^{1/2}$ [at electrode potentials (V): –0.4 (*1, 2*) and 0.2 (*3, 4*)]; (b) $C_P$ and (c), (d) $R_P$ vs. a.c. frequency plots [at electrode potentials (V): 1.1 (*1*), 0.2 (*2*), –0.2 (*3*) and –0.4 (*4*)] for the DLCE|$x$M NaF+$H_2O$ interface [$x$=0.1 (a, c), 0.01 (b) and 0.001 (d)].

At $\nu \ge 1000$ Hz, the values of $C_S$ and $C_P$ are of the same order as the values obtained for the flat single-crystal Bi, Ag and Cd electrodes [62–65]. Thus, in this region of $\nu$, where the a.c. penetration depth is small, the surface of the DLCE seems to be comparatively flat (the DLCE surface works as a flat surface). In the region $\nu < 100$ Hz, a very high increase of $C_S$ as well as $C_P$

values takes place and thus very high capacitance values, compared with the smooth single-crystal metal electrodes, have been established at $\nu \approx 0.1$ Hz. Thus, at higher a.c. penetrability the DLCE surface demonstrates parameters that are characteristic for very rough electrodes. However, the values of $C_S$ for the DLCE are ~$10^3$–$10^5$ times lower than for the NPCE [6]. The very weak dependence of $C_S$ on $E$ as well as the good agreement of $C_S$ and $C_P$ values in the region $-0.2 < E < 1.1$ V and the very high parallel resistance $R_P$ values (Fig. 29c) indicate the absence of rapid faradaic processes at the DLCE|$x$M NaF+$H_2O$ interface. Comparison of $Z`$, $C_S$, $C_P$, $|Z|$ and $\delta$ vs. log$\nu$ dependences obtained at different electrolyte concentrations indicate that the solution phase characteristics (i.e. the electrolyte resistance, Debye screening length and diffuse layer capacitance) are very important parameters for obtaining the high-frequency characteristics (series resistance) of the DLCE|$x$M NaF+$H_2O$ interface. According to the data in figure 29c and d, the values of the parallel resistance $R_P$ as well as the series resistance $R_S$ noticeably decrease with the increase of electrolyte concentration. The very high $R_P$ values indicate that there is no rapid faradaic processes at $-0.3 < E < 1.0$ V.

## 6.6. Fitting results of the experimental complex plane plots

Usually the $Z``$ vs. $Z`$ plots, like those presented in figures 26a, 27a and 28a, have been simulated by the Randles-type equivalent circuit (circuit I in Fig. 30) that combines the high-frequency resistances of the electrode material and bulk electrolyte ($R_{el}$), the electrical double layer and adsorption capacitances ($C_{dl}$ and $C_{ad}$), the ionic charge transfer resistance ($R_{ad}$) and double layer resistance ($R_{dl}$) at the front contact and the restricted diffusion (Warburg-like impedance, $Z_W$) of the adsorbed or inserted species (the insertion of $H^+$ as well as $Na^+$ cations in our case) into the electrode material from aqueous and non-aqueous solutions [75–84]. In this case, the specific impedance and capacitance functions have the following forms:

$$Z(\omega) = R_{el} + \frac{1}{j\omega C_{dl} + \dfrac{1}{\dfrac{C_{ad}}{\sqrt{j\omega}} + \dfrac{1}{j\omega C_{ad}} + R_{ad}}} \tag{1}$$

and

$$C(\omega) = \frac{1}{j\omega\left[Z(\omega) - R_{el}\right]} = C_{dl} + \frac{C_{ad}}{1 + \sigma_{ad} C_{ad} \sqrt{j\omega + R_{ad} C_{adj\omega}}} \tag{2}$$

where $\sigma_{ad}(j\omega)^{-1/2}$ represents the diffusion (Warburg-like) impedance $Z_W$ with its coefficient $\sigma_{ad}$. Studying the difference between the equivalent circuits presented in figure 30, there are two accurate ways to obtain an indication of how well the modelling function reproduces the experimental data set: (1) observing the parameter values and their relative error estimate (in %); (2) the chi-squared function ($\chi^2$) also gives a good indication of the quality of the fit [74, 84–87].

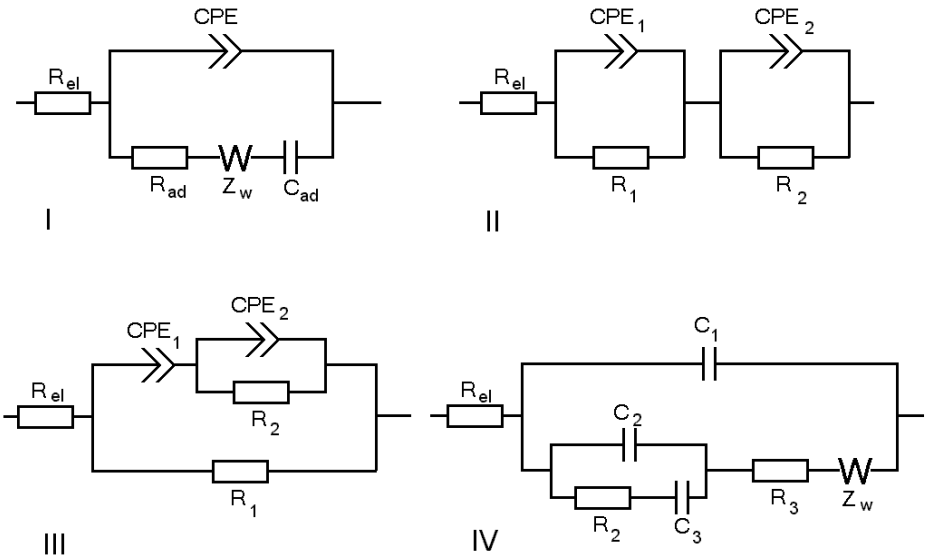


**Figure 30.** Equivalent circuits used for fitting the experimental complex plane plots. *I*: modified Frumkin-Melik-Gaikazyan and Randles circuit, where CPE is the constant phase element, $R_{ad}$ is the charge transfer resistance, $Z_W$ is the Warburg-like diffusional impedance, and $C_{ad}$ is the adsorption capacitance. *II*: circuit consisting of two CPE elements ($CPE_1$ and $CPE_2$) in parallel with the resistances $R_1$ and $R_2$ (see text). *III*: circuit in which $R_{el}$ is the resistance of the electrolyte and DLCE material; $CPE_1$ is the constant phase element related to the capacitance of the Helmholtz layer and surface films; and $CPE_2$ is related to the capacitance of the flat electrode|electrolyte interface; $R_1$ is the charge transfer resistance of the flat electrode|solution interface; and $R_2$ is the partial charge transfer resistance at the internal surfaces of a rough electrode. *IV*: circuit in which $R_{el}$ is the resistance of the electrode material and bulk electrolyte; $C_1$, $C_2$ and $C_3$ are the surface film, double layer and adsorption capacitances; and $R_2$ and $R_3$ are the charge (or partial charge) transfer and surface film resistances, respectively.

The results of fitting of experimental $Z``$ vs. $Z`$ plots (Fig. 31a), using the program Zview 2.2 for Windows, shows that the agreement is not very good at smaller frequencies $\nu < 5$ Hz ($\chi^2 \geq 1.5\times10^{-3}$ and the weighted sum of squares is $\Delta^2 \geq 0.14$). Therefore, this simple model seems to be valid for the DLCE|*x*M $NaF+H_2O$ interface only to a first very rough approximation. The model of Ho et al. [85] is a modification of the Frumkin-Melik-Gaikazyan-Randles-type

model and it predicts pure capacitive behaviour at low frequencies. However, in good agreement with the results of other studies [5, 6], the impedance is not purely capacitive for the DLCE|*x*M NaF+$H_2O$ interface at $v < 5$ Hz. Our results (Figs. 26, 27, 28, 29) show that a certain capacitance dispersion characteristic of polycrystalline solid electrodes has been observed and, in such cases, the impedance spectra ($Z$ vs. $\omega$) can be modelled by an equivalent circuit containing a constant phase element (CPE) showing power law frequency dependence:

$$Z_{CPE}(\omega) = A^{-1}(j\omega)^{-\alpha} \tag{3}$$

where $\omega$ is the angular frequency and $j = \sqrt{-1}$. According to the experimental results obtained for various metal electrodes, the smoother and cleaner the surface, the closer is the value of α to unity (at α = 1.0, the value of the CPE coefficient $A$ is equal to the capacitance of the double layer, but in the general case the frequency-independent coefficient $A$ has the dimensionality $F^{\alpha}\ \Omega^{\alpha-1}\ cm^{-2}$). The dependences of $A$ and α on $E$ obtained for different electrolyte concentrations are given in figure 31b. The value of α somewhat decreases with dilution of the electrolyte, in the same direction as the constant $A$. The adsorption capacitance $C_{ad}$ increases with $c_{NaF}$ as well as with the negative polarization of the electrode, which can be explained by the more pronounced adsorption of $Na^+$ ions (and probably noticeable intercalation at $E \leq -0.4$ V) on the DLCE surface (Fig. 31c). This dependence is in good agreement with the decrease of the partial charge transfer resistance (or the "true" faradic change transfer reaction resistance) (Fig. 31c) and diffusion resistance values ($R_D$) (Fig. 31d), obtained according to the generalized finite Warburg element (GFW) for a short circuit terminus model, expressed as:

$$Z_{GFW}=R_D\tanh[(jT\omega)^{\alpha W}](jT\omega)^{-\alpha W} \tag{4}$$

where $R_D$ is the so-called limiting diffusion resistance; the so-called frequency parameter $T = L^2/D$, where $L$ is the effective diffuse layer thickness and $D$ is the effective diffusion coefficient of a particle; $\alpha_W$ is a fractional exponent, varying from 0 to 1. Values of $\alpha_W$ somewhat higher than 0.5 ($0.53 \leq \alpha_W \leq 0.63$) (Fig. 31d) indicate that there are small deviations of the DLCE|*x*M NaF+$H_2O$ interface from the classical semi-infinite diffusion layer model with $\alpha_W$ =0.5 [86–89].

The analysis of the $Z``$ vs. $Z`$ plots shows that the DLCE|*x*M NaF+$H_2O$ interface can be simulated with better accuracy by an equivalent circuit (circuit 2 in Fig. 30) which consists of two CPE elements ($CPE_1$ and $CPE_2$) in parallel with the resistances $R_1$ and $R_2$. According to the results of fitting (Fig. 32a) ($\chi^2 \leq 1.3\times10^{-3}$ and $\Delta^2 \leq 0.1$), the first block of this circuit formally describes the high-frequency parameters of the DLCE|electrolyte interface, which seems “flat” at higher frequencies (at low a.c. penetration steps) and the second parallel combination of $CPE_2$ and $R_2$, describes the electrical double layer (interfacial) parameters at low frequencies (i.e. mainly Helmholtz inner layer characteristics at rough internal surfaces of the DLCE).

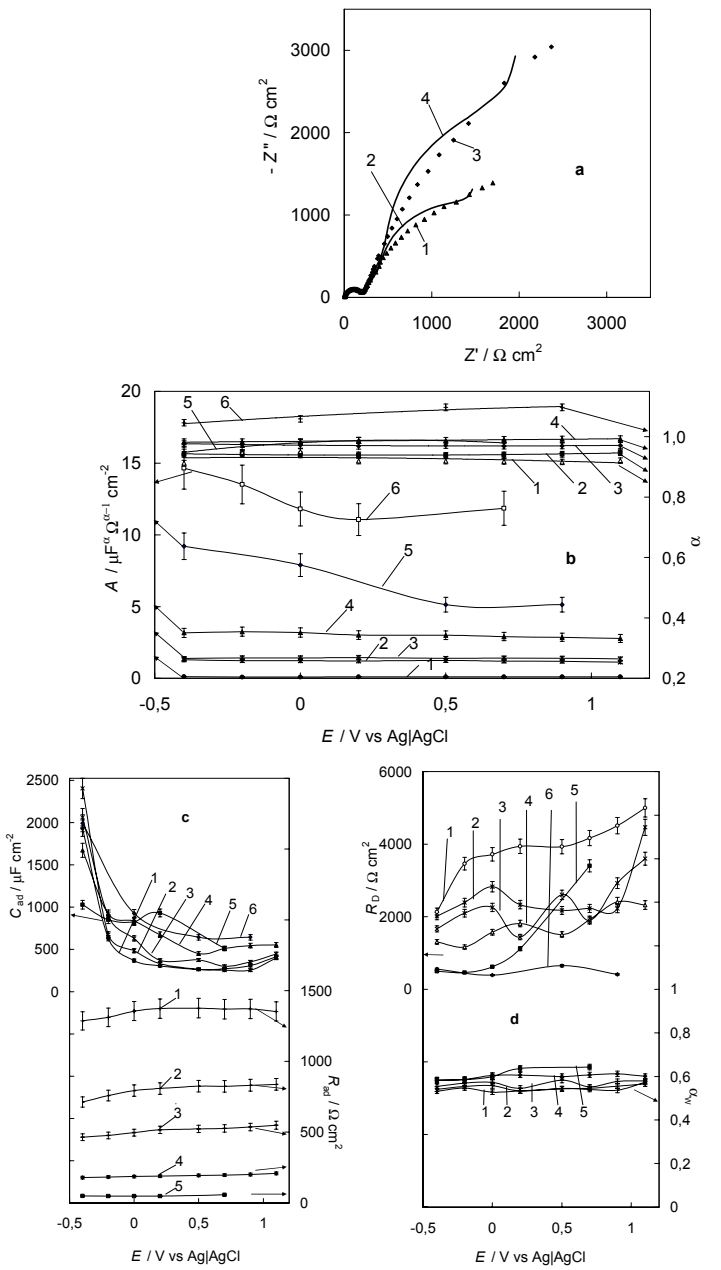


**Figure 31.** (a) Experimental $Z``$ vs. $Z`$ plots (*points*) (*1*, *3*) for the DLCE|0.01 M NaF+$H_2O$ interface and calculated curves according to the Frumkin-Melik-Gaikazyan and Randles model (*solid lines*) (*2*, *4*) at electrode potentials (V) of –0.4 (*1*, *2*) and 0.2 (*3*, *4*). (b) CPE coefficient $A$ and fractional exponent α vs. electrode potential plots; (c) $C_{ad}$ and $R_{ad}$ vs. electrode potential plots; and (d) $\alpha_W$ and $R_D$ vs. electrode potential plots for the DLCE|$x$M NaF+$H_2O$ interface with the following values of $x$: 0.001 (*1*), 0.002 (*2*), 0.003 (*3*), 0.01 (*4*), 0.05 (*5*) and 0.1 (*6*).

The results of the simulations show that there is a very well pronounced dependence of the values of $A_1$, $A_2$ (obtained from $CPE_1$ and $CPE_2$, respectively), $R_1$ and $R_2$ on the electrolyte concentration (Fig. 32b and c). For example, the parallel resistance of the so-called high-frequency part of the equivalent circuit ($R_2$) noticeably increases with the decrease of the electrolyte concentration, and the same is valid for $A_2$ and $\alpha_2$ (obtained from $CPE_2$) according to Eq. 3. Except for $A_2$ values at higher electrolyte concentrations, the values of $A_2$, $\alpha_2$ and $R_2$ are practically independent of the electrode potential and probably characterize the bulk electrolyte as well as the bulk electrode material characteristics. The value of $A_2$ noticeably decreases with the decrease of the electrolyte concentration and the very low values of $A_2$ for $c_{NaF} < 1\times10^{-2}$ M [5, 6], compared with metal electrodes, probably indicate the very large influence of the potential drop in the surface layer of the DLCE (i.e. the main potential drop is attributed to the space charge region within the DLCE) [90–92].

The values of $A_1$, related to $CPE_1$, are noticeably higher than $A_2$, which can be explained by the fact that the a.c. penetration depth is high at low frequencies and the whole surface of the rough DLCE participates actively in the electrical double layer formation process. The noticeable increase of $A_1$ with the negative polarization of the DLCE (Fig. 32b) can be explained by the weak adsorption of the $Na^+$ cations on the internal surface of the DLCE. The noticeably lower values of $\alpha_1 \leq 0.7$ compared with $\alpha_2 \geq 0.90$ indicate that the DLCE surface is geometrically inhomogeneous, as well as by the fact that the deviation of the system from purely capacitive behaviour ($\alpha$=1) toward diffusion-limited behaviour ($\alpha$=0.5) increases. Thus, the noticeable increase of $A_1$ and decrease of the parallel resistance $R_1$, as well as the fractional exponent $\alpha_1$, probably indicate an increase in the rate of the partial charge transfer process (or "true" faradaic cathodic process resistance) with the negative polarization.

Taking into account the fact that there is a potential drop in the surface layer of the DLCE, the equivalent circuit III, presented in figure 30, has been used for fitting the experimental Z`` vs. Z` plots. In this circuit, $R_{el}$ is the cell resistance, including the resistances of the bulk DLCE film and the bulk electrolyte solution; $CPE_1$ is the constant phase element related to the constant $A_1$ and $\alpha_1$ (i.e. with capacitance $C_1$ if $\alpha_1$=1.0) corresponding to the elements (i.e. potential drops) which are located outside the semiconductor (e.g. to the various surface films and Helmholtz layer capacitance of the rough energetically and geometrically inhomogeneous surface of the DLCE, characterized by the fractional exponent $\alpha_1$). In our case, $CPE_2$ is the frequency-dependent element with the constant phase angle (characterized by $A_2$ and $\alpha_2$) that describes the relaxation process occurring on the electrode surface and/or in the space charge region; $R_2$ is the resistance characterizing the charge transfer process at the (internal) electrode surface regions, i.e. the resistance of the intercalation process of cations ($Na^+$ and/or $H^+$ ions); $R_1$ is the parallel resistance for the "true" faradaic or partial charge transfer process at the macroscopically flat DLCE|solution interface. Analysis of the complex plane plots (Figs. 26, 27, 28) shows that the DLCE|*x*M $NaF+H_2O$ interface can be simulated with a good accuracy

($\chi^2 \leq 7\times10^{-4}$ and $\Delta^2 \leq 0.05$) (Fig. 33a) using the equivalent circuit III presented in figure 30. The parameters obtained from the fitting of the Z`` vs. Z` plots of the DLCE|*x*M NaF+$H_2O$ interface are given in figure 33b and c.

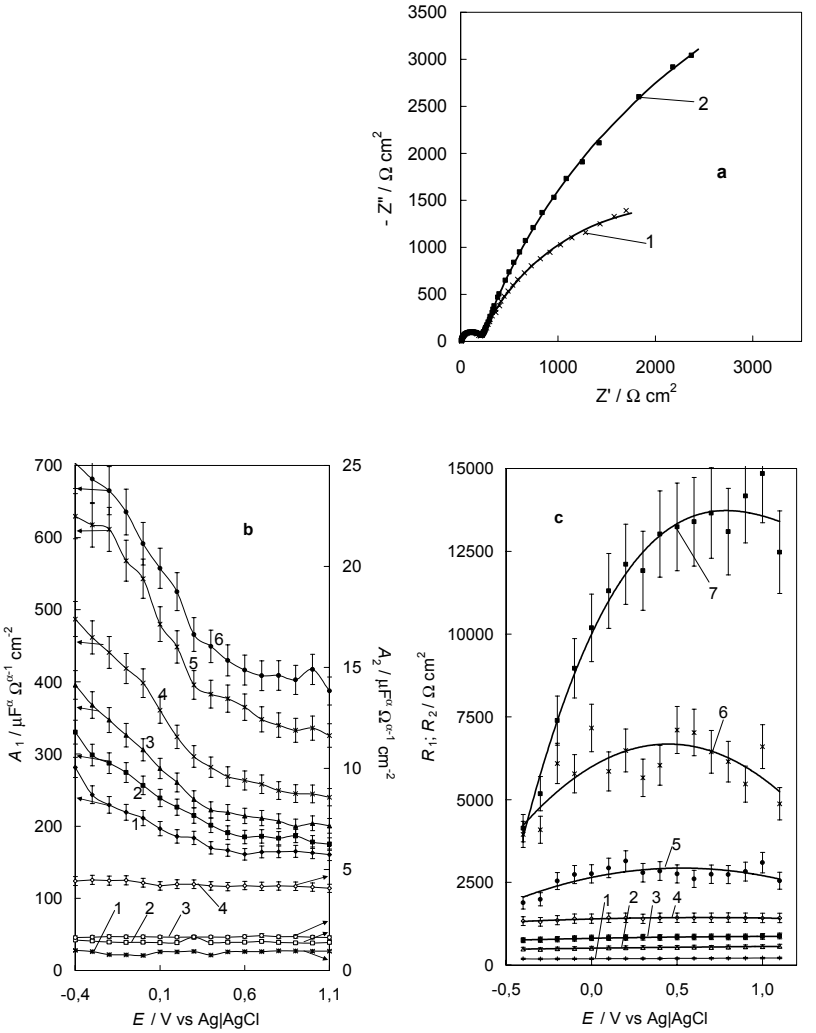


**Figure 32.** (a) Experimental Z`` vs. Z` plots (*points*) for the DLCE|0.01 M NaF+$H_2O$ interface and calculated curves (lines) according to the equivalent circuit II in figure 30 (where $CPE_1$ and $R_1$ are the constant phase element and resistance, corresponding to the high-frequency region, and $CPE_2$ and $R_2$ characterize the low-frequency behavior of the system) at electrode potentials (V) of –0.4 (*1*) and 0.2 (*2*). (b) $A_1$ and $A_2$ and (c) and $R_1$ (*5–7*) and $R_2$ (*1–4*) versus electrode potential plots for the DLCE|*x*M NaF+$H_2O$ interface with the following values of *x* for (b): 0.001 (*1*), 0.002 (*2*), 0.003 (*3*), 0.01 (*4*), 0.05 (*5*) and 0.1 (*6*); and for (c): 0.01 (*1*), 0.003 (*2*), 0.002 (*3*), 0.001 (*4*), 0.1 (*5*), 0.05 (*6*) and 0.01 (*7*).

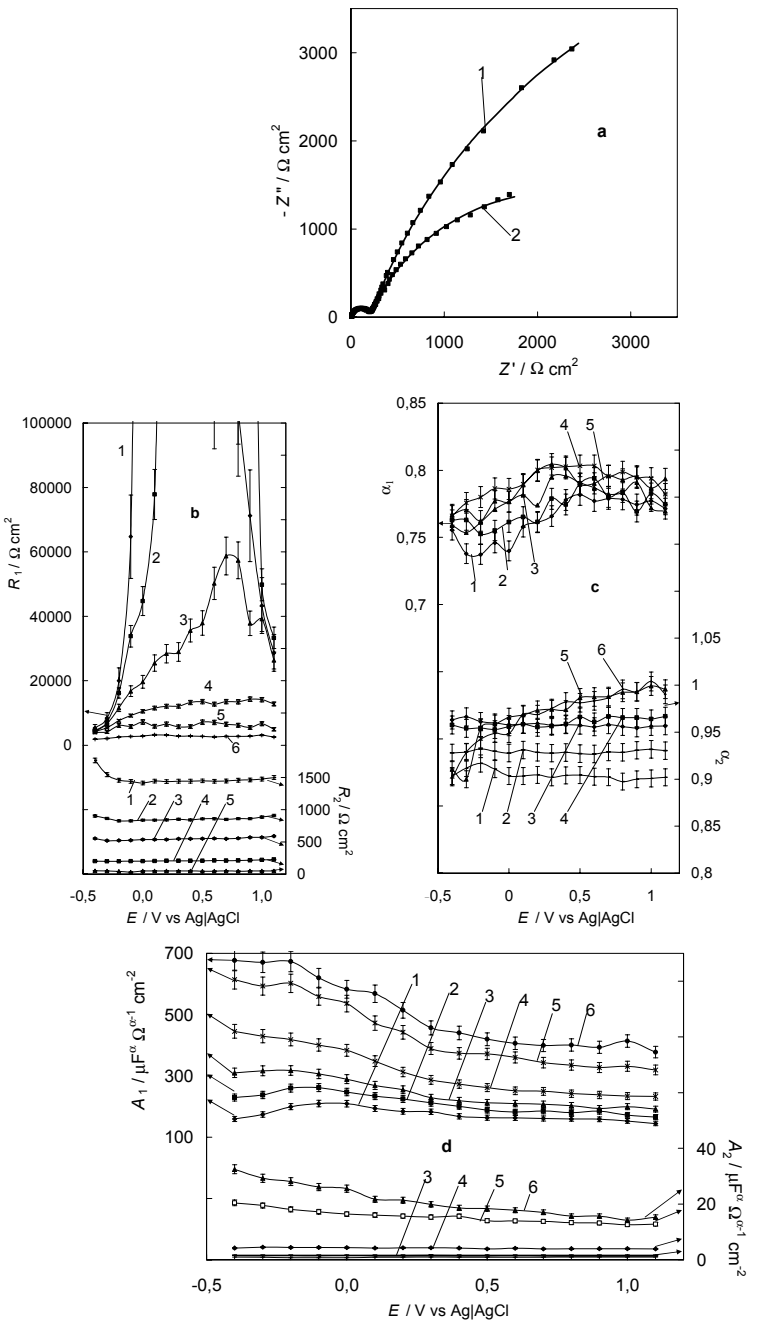


**Figure 33.** (a) Experimental Z`` vs. Z` plots (*points*) for the DLCE|0.01 M NaF+$H_2O$ interface and curves calculated according to the equivalent circuit III (*lines*) at the following electrode potentials (V): 0.3 (*1*) and –0.3 (*2*). (b) $R_1$ and $R_2$, (c) $\alpha_1$ and $\alpha_2$ and (d) $A_1$ and $A_2$ vs. electrode potential plots for the DLCE|*x*M NaF+$H_2O$ interface with the following values of x: 0.001 (*1*), 0.002 (*2*), 0.003 (*3*), 0.01 (*4*), 0.05 (*5*) and 0.1 (*6*).

According to these data, there is a noticeable dependence of $R_1$ and $R_2$ on the electrolyte concentration (Fig. 33b), as well as, for the more dilute electrolyte solutions, on the electrode potential. $R_1$ and $R_2$ increase noticeably with dilution of the electrolyte, but the values of $R_1$ are two orders higher than $R_2$ values. The very high $R_1$ values indicate that the influence of the parallel resistance $R_1$ (i.e. resistance of charge transfer or partial charge transfer on the macroscopically flat surface) is not important and, to a first very rough approximation, $R_1$ can be neglected in circuit III in figure 30. The noticeably lower values of $\alpha_1$, compared with $\alpha_2$, probably indicate the influence of the geometrical surface roughness and therefore the surface energetic inhomogeneity [i.e. dependence of the zero charge potential on various surface regions with different electronic states ($sp^3$ or $sp^2$ hybridization)] on the electrical double layer characteristics [i.e. interfacial Helmholtz and diffuse layer characteristics (capacitance, charge density), and capacitance and resistance parameters of various surface films, etc.] for the DLCE|*x*M $NaF+H_2O$ interface. The small decrease of $\alpha_1$ with increasingly negative polarization can be explained by the increase of the rate of the faradaic (or partial charge transfer) reaction. The constant $A_2$ related to $CPE_2$ clearly depends on the electrolyte concentration and for a $c_{NaF} \geq 5\times10^{-2}$ M solution $A_2$ somewhat increases with the increase of the negative polarization of the DLCE. The values of $A_1$, related to $CPE_1$, are noticeably higher compared with the values of $A_2$, but the dependence of $A_1$ on $c_{NaF}$ is more pronounced and, thus, the Helmholtz layer capacitance and/or capacitance of the surface films clearly depend on the surface charge density. This result is in good agreement with the lower values of $\alpha_1$ (i.e. the fractional exponent of the Helmholtz layer and/or surface films) and its decrease with the increase of negative polarization. Thus, with the increase of the negative surface charge density, the deviation of the DLCE|*x*M $NaF+H_2O$ interface from the "flat" nearly ideally polarizable interface increases. Comparison of the values of $A_1$ with $A_2$ and $R_1$ with $R_2$ obtained using the equivalent circuits II and III shows that the influence of the resistance $R_1$ in circuit III on the other parameters obtained is very small at $0.1 < E < 1.1$ V (because of the very high parallel resistance values) and therefore this equivalent circuit III can be simplified by neglecting the $R_1$ value. A good agreement between the $A_1$, $A_2$, $\alpha_1$, $\alpha_2$ and $R_2$ values obtained using circuits II and III gives some evidence that the values are quite realistic.

It should be noted that the excellent agreement between the simulations and the experimental data ($\chi^2 \leq 3\times10^{-4}$ and $\Delta^2 \leq 0.03$) for the DLCE|*x*M $NaF+H_2O$ interface has been established if circuit IV in figure 30 is used, in which the charge transfer and double layer charging at the surface, the intercalation of $Na^+$ or $H^+$ ions and solid phase diffusion inside the nanoparticle (i.e. in the nearly spherical particle; see AFM data in Fig. 24), as well as the effect of an insulating film at the surface (i.e. surrounding of the nanoparticles), have been taken into account [79, 80]. In this circuit, $R_{el}$ is the series resistance, including the resistance of the bulk diamond film and bulk electrolyte solution; $C_1$ is the capacitance of the surface film, developed on the surface of the DLCE and described as a simple dielectric by Eq. 5:

$$C_1 = \varepsilon_f h_f^{-1} \quad (5)$$

where $\varepsilon_f$ is the permittivity and $h_f$ is the thickness of a diamond-like carbon film with resistance $R_3$. According to the results of the simulations, the capacitance of this film is comparatively small, but if the film is a dielectric, it is possible to separate the charge across it. Only at a very high frequency there will be a significant current flow due to separation of charges across the film, resulting in "shorting" the resistance of the film [80]. $C_2$ is the so-called interfacial (i.e. double layer) capacitance, which is caused by charging and discharging the electrical double layer at the internal surfaces of the rough electrodes; $R_2$ is the partial charge transfer or "true" faradaic reaction resistance of the film; $C_3$ is the adsorption capacitance; $Z_W$ is the Warburg-like diffusion impedance, simulated using the Frumkin-Melik-Gaikazyan semi-infinite diffusion model ($\alpha_W$=0.5) [88, 89] or by the generalized finite length Warburg short circuit model [86, 87].

The results of the simulations given in figure 34b-d indicate that the surface film capacitance $C_1$ is small in comparison with the "true" double layer capacitance $C_2$ and adsorption capacitance $C_3$. The high values of $C_2$ and $C_3$ are caused mainly by the very rough internal surface structure of the DLCE as well as by the weak adsorption of $Na^+$ ions, increasing with the increase of the negative surface charge density of the DLCE surface (Fig. 34c and d). The resistance of the surface film, $R_3$ (Fig. 34e), is smaller than corresponding values established by Meyers et al. [80] and therefore the conductivity of the surface films is higher. The partial charge transfer or "true" faradaic process resistance $R_2$ values are larger (Fig. 34f) compared with the results of Meyers et al. [80], and therefore the rate of the probable intercalation process of $H^+$ or $Na^+$ ions into the DLCE is smaller.

The fitting results for the DLCE|*x*M NaF+$H_2O$ interface show that the so-called external impedance $Z_{ext}$, obtained by the parallel combination of external resistance $R_{ext}$ and capacitance $C_{ext}$ circuit elements [80], has to be replaced by the Warburg-like diffusion impedance $Z_W$, calculated according to Eq. 4. The fitting data show that the diffusion resistance $R_D$ (Fig. 35a) decreases with the increase of electrolyte concentration as well as of the negative polarization. The values of the fractional exponent $\alpha_W$ in Eq. 4 are very close to 0.5 (Fig. 35b) and, to a first approximation, the classical semi-infinite diffusion layer model seems to be applicable for the DLCE|*x*M NaF+$H_2O$ interface.

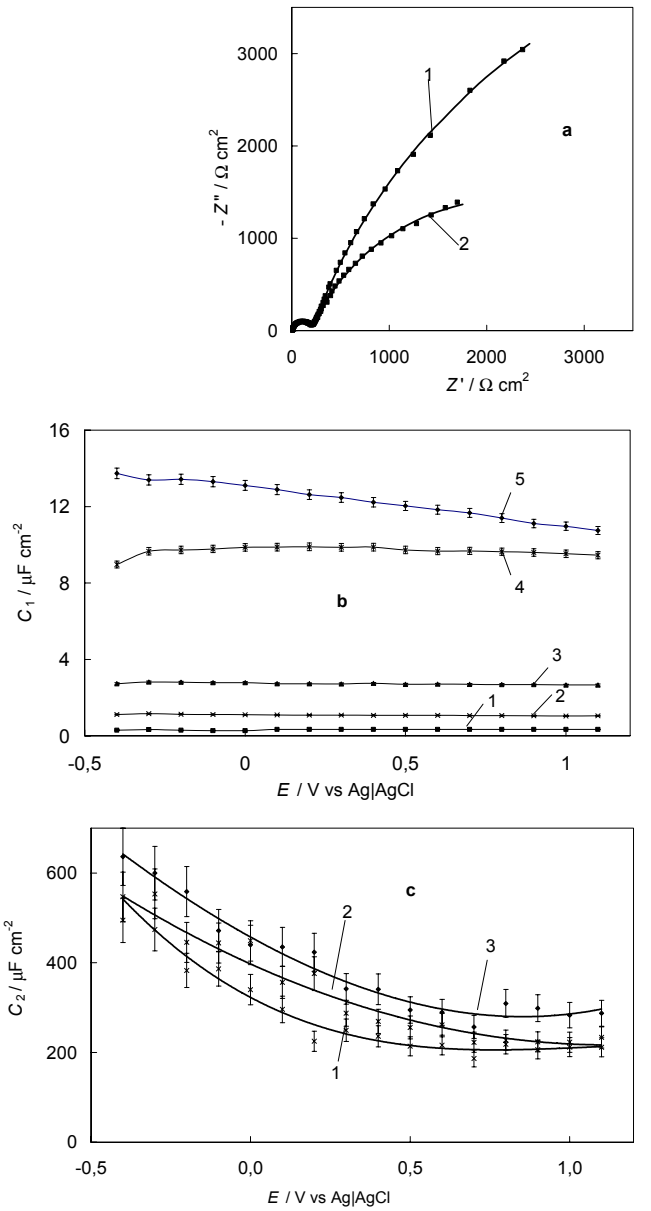


**Figure 34.** (a) Experimental Z`` vs. Z` plots for the DLCE|0.01 M NaF+$H_2O$ interface (*points*) and curves (*solid lines*) calculated according to the equivalent circuit IV (in Fig. 30) at the following electrode potentials (V): 0.3 (*1*) and –0.3 (*2*). (b) $C_1$ vs. $E$ curves [at the following values of $x$: 0.001 (*1*), 0.002 (*2*), 0.01 (*3*), 0.05 (*4*) and 0.1 (*5*)], (c) $C_2$ versus $E$ plots [$x$: 0.003 (*1*), 0.05 (*2*) and 0.1 (*3*)], (d) $C_3$ vs. E curves [$x$: 0.001 (*1*), 0.003 (*2*), 0.01 (*3*), 0.05 (*4*) and 0.1 (*5*)], (e) $R_3$ vs. $E$ curves [$x$: 0.001 (*1*), 0.003 (*2*), 0.05 (*3*) and 0.1 (*4*)], and (f) $R_2$ vs. $E$ plots [$x$: 0.003 (*1*), 0.01 (*2*), 0.05 (*3*) and 0.1 (*4*)] for the DLCE|$x$M NaF+$H_2O$ interface.

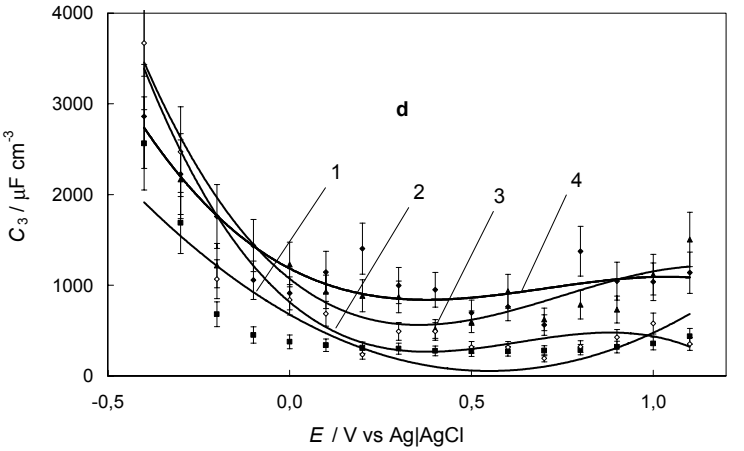


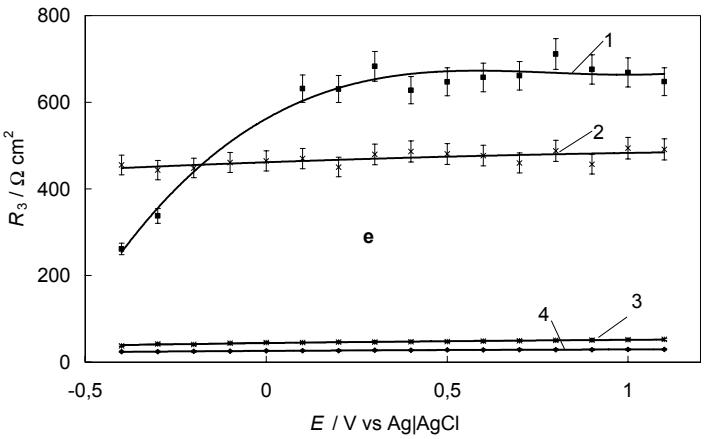


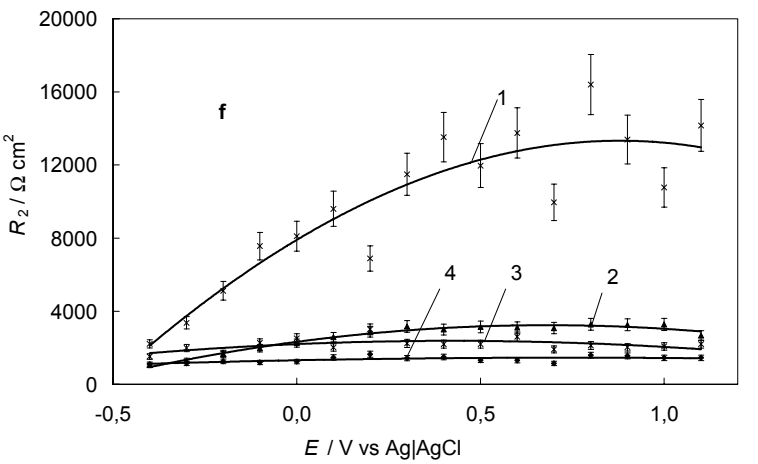


**Continued figure 34.**

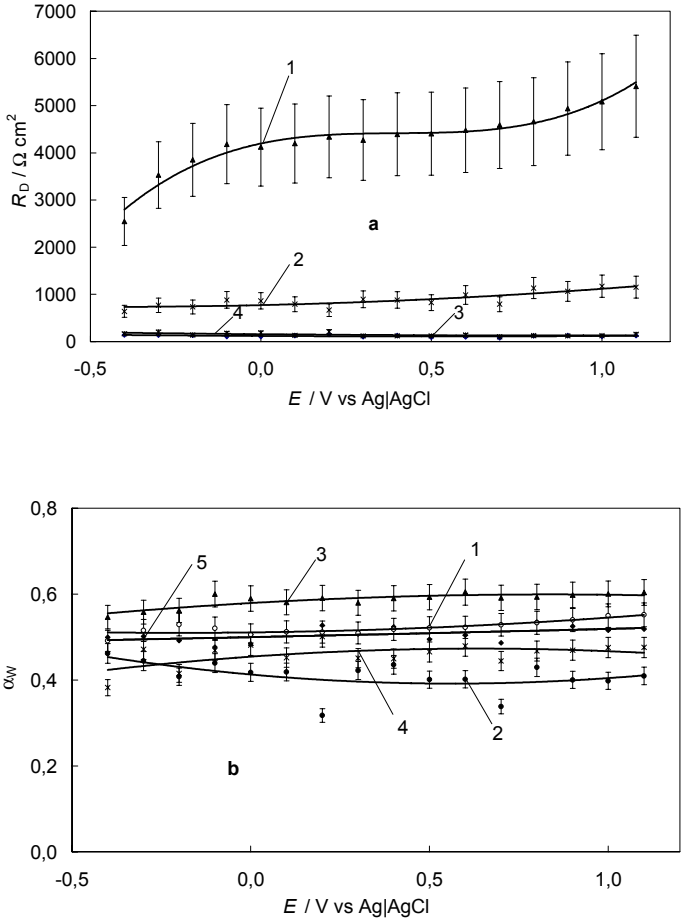


**Figure 35.** (a) $R_D$ vs. $E$ plots [$x$: 0.001 (*1*), 0.003 (*2*), 0.05 (*3*) and 0.1 (*4*)] and (b) $\alpha_W$ vs. $E$ plots [$x$: 0.001 (*1*), 0.003 (*2*), 0.01 (*3*), 0.05 (*4*) and 0.1 (*5*)] for the DLCE|$x$M NaF+$H_2O$ interface.

# 7. SUMMARY

Various diamond-like carbon (DLC) films were prepared using four different type synthesis setups. The setup No. 1 included a very miniature vacuum chamber, which interchangeable laser window served also as a deposition substrate (exposed to the laser irradiation). The setups Nos. 2, 3 and 4 included the vacuum chamber with cooled liquid target holder and heated substrate holder, constructed specially in this work. In the setup No. 2, a semitransparent mirror was used additionally for substrate excitation. In the setup No. 3, the applied laser was operating periodically between the deposition and excitation pulses by a movable mirror. The main difference in setup No. 4 was that different substrates – carbon sticks (surrounded on the lateral sides by a polystyrene film and additionally isolated by a Teflon holder) – were used, instead of a fused silica plates. Synthesized film characteristics were obtained by optical microscopy, Raman spectroscopy, atomic force microscopy (AFM) and by electrochemical measurements.

The Raman spectroscopy data of carbon films, which were synthesized in miniature vacuum chamber (setup No. 1), showed that the films grown in $H_2O_2$ flow (0.02 – 1.2 mbar) had high content of $sp^3$ bonded carbon (we conservatively estimate the average $sp^3/sp^2$ bonding ratio to be higher than 50%). Optical microscopy data showed that the film regions grown under excimer laser illumination were strongly interference colored at certain energy densities of illumination. This was in contrast with the grey or brown regions grown without laser illumination, and shows that DLC films with a very wide bandgap ($\Delta E > 3$ eV) can be grown under laser illumination conditions at room temperature. AFM measurements indicated that the DLC films grown under laser illumination conditions were smoother, and especially smooth surfaces were observed for the colored films (particles) deposited inside the laser beam irradiated surface regions.

Raman spectroscopy studies of films indicated that higher ablating laser beam intensity had positive influence on the $sp^3$ hybridized carbon content in films (setup No. 2). Influence of $H_2O_2$ vapor on these film parameters can be described as increasing the number of ordered aromatic carbon rings with decreasing size of the aromatic clusters in DLC films. The results of Raman spectroscopy studies indicated that at higher substrate temperatures the Raman spectra G band shifts towards higher frequency, which demonstrates preferable $sp^3$-hybridized carbon transformation to the $sp^2$-hybridized carbon structure. The dependence of the G band Raman shift on substrate temperature was quite linear.

AFM studies indicated that lower deposition temperatures resulted in bigger grain size of the DLC film surface structures. A sudden drop in the root mean square (RMS) roughness value has been observed in a relatively narrow range of temperature from 50 to 100ºC applied. At higher temperatures the RMS did not change noticeably and approached to a plateau.

Raman scattering data indicated that the additional irradiation of the growing film between the ablation pulses (setup No. 3) is inevitable to create the individual diamond phase formation into DLC films. The existence of diamond clusters in these films was also confirmed using AFM method. The individual diamond phase forms only in a narrow window of irradiating laser beam energy density. At lower energy densities the irradiation promoted the growth of homogeneous DLC structures with high content of $sp^3$ hybridized carbon. However, at higher laser irradiation intensities the DLC phase decomposition and graphitization takes place.

The cyclic voltammetry and impedance data for the DLCE|*x*M NaF+$H_2O$ interface show that this system is nearly ideally polarizable in the potential region $-0.4 < E < 1.1$ V [vs. AgCl|Ag (sat. KCl in $H_2O$)]. For materials tested the RMS roughness is 81 Å and the medium size of a DLCE particle is about 0.1 μm (established by AFM). The shape of complex plane plots depends on the electrode potential and noticeably on the electrolyte concentration. The non-linear least squares fitting method of the experimental data shows that various equivalent circuits can be used for fitting the experimental impedance complex plane plots. An excellent fit has been established using a circuit combining the total high frequency series resistance $R_{el}$ of the electrode system, including the resistance of the bulk diamond film and bulk electrolyte solution, the capacitance $C_1$ and the resistance $R_3$ of the surface film, developed on the surface of the DLCE, the so-called interfacial (i.e. double layer) capacitance $C_2$ (caused by the charging and discharging of the electrical double layer at the internal surface of DLCE), the partial or "true" faradaic reaction resistance of the film $R_2$, the low frequency adsorption capacitance $C_3$ and the Warburg-like diffusion impedance $Z_W$.

The distributed nature of the impedance (at low frequency) results in just an engagement of the available surface area. Rather than passing current through only a single particle, current passes through all of the particles in the rough or porous electrode without any noticeable additional ohmic drop. The ohmic drop in the solution phase for the systems simulated greatly affects the overall impedance of the rough (porous) electrode, increasing its magnitude and decreasing its phase angle. It is clear that the breadth of the particle-size distribution affects the solid-phase diffusion impedance, except in its high-frequency limit. The low-frequency limit yields no useful information about the diffusion coefficient in the solid unless the particle-size distribution is well known.

# 8. REFERENCES


[1] N. Benchikh, F. Garrelie, C. Donnet, K. Wolski, R.Y. Fillit, F. Rogemond, J.L. Subtil, J.N. Rouzaud, J.Y. Laval, Surf. and Coat. Techno. 200 (2006) 6272.

[2] S.M. Mominuzzaman, T. Soga, T. Jimbo, M. Umeno, Thin Solid Films 376 (2000) 1.

[3] J.M. Lackner, C. Stotter, W. Waldhauser, R. Ebner, W. Lenz, M. Beutl, Surf. and Coat. Technol. 174–175 (2003) 402.

[4] P.M. Ossi, C.E. Bottani, A. Miotello, Thin Sol. Films 482 (2005) 2.

[5] B.E Conway, Electrochemical supercapacitors: scientific fundamentals and technological applications. Kluwer/Plenum, New York (1999) 1.

[6] E. Lust, G. Nurk, A. Jänes, M. Arulepp, P. Nigu, L. Permann, P. Möller, J. Condens. Mater. Phys. 2 (2002) 1.

[7] R. Kalish, Carbon 37 (1999) 781.

[8] Y.V. Pleskov, A.Y. Sakharova, M.D. Krotova, L.L. Bouilov, B.V Spitsyn, J. Electroanal. Chem. 228 (1987) 19.

[9] Y.V. Pleskov, Y.E. Evstefeeva, M.D. Krotova, V.V. Elkin, V.M. Mazin, V.Y. Mishuk, V.P. Varin, I.G. Teremetskaya, J. Electroanal. Chem. 455 (1998) 139.

[10] G. Janssen, W.J.P. van Enckevort, W. Wollenberg, L.J. Giling, Diamond Relat. Mater. 1 (1992) 789.

[11] P. Ball, Nature 381 (1996) 116.

[12] J. van de Lagenmaat, D. Vanmaekelbergh, J.J. Valley, J. Electroanal. Chem. 475 (1999) 139.

[13] W. Kulish, Deposition of diamond-like superhard materials. Springer, Berlin Heidelberg New York, (1999) 1.

[14] M. Tabal, P. Mérel, M. Chaker, M.A. El Khakani, E.G. Herbert, M.B. Lucas, M.E. O'Hern, Surf. Coating. Technol. 116 (1999) 452.

[15] Y.Y. Tsui, D.G. Redmon, Surf. Coat. Technol. 126 (2000) 96.

[16] Q. Wei, J. Samkar, A.K. Sharma, Y. Yamagata, J. Narayan, J. Vacuum Sci. Technol. A 19 (2001) 311.

[17] K. Ebihara, T. Nakamiya, T. Ohshima, T. Ikegami, S. Aoqui, Diamond Relat. Mater. 10 (2001) 900.

[18] K. Okada, T. Aizawa, R. Souda, S. Komatsu, S. Matsumoto, Diamond Relat. Mater. 10 (2001) 1991.

[19] Q. Wei, J. Sankar, J. Nakayan, Surf. Coat. Tech. 146–147 (2001) 250.

[20] J. Robertson, Mater. Sci. Eng. Res. Rep. 37 (2002) 129.

[21] J. Gao, Int. Mod. Phys. B 16 (2002) 1024.

[22] S. Fedosenko, D. Korzec, J. Engemann, D. Lyebyedyev, H.C. Scheer, Thin Solid Films 406 (2002) 275.

[23] A.C. Ferrari, Diamond Relat. Mater. 11 (2002) 1053.

[24] T.N. Rao, D.A. Tryk, K. Hashimoto, A. Fujishima, J. Electrochem. Soc. 196 (1999) 680.

[25] I. Yagi, K. Tsunosaki, D.A. Tryk, A. Fujishima, Electrochem. Solid State Lett. 2 (1999) 457.

[26] D.R. McKenzie, D. Muller, B.A. Pailthorpe, Phys. Rev. Lett. 67 (1990) 773.

[27] A. Ilie, A.C. Ferrari, T. Yagi, J. Robertson, Appl. Phys. Lett. 76 (2000) 2627.

[28] A.A. Voevodin, M.S. Donley, J.S. Zabinsky, J.E. Bultman, Surf. Sci. Coat. Technol. 77 (1995) 534.

[29] M.P. Siegal, D.R. Tallant, P.N. Provencio, D.L. Overmyer, R.L. Simpson, Appl. Phys. Lett. 76 (2000) 3052.
[30] A. Grill, V. Patel, Diamond Relat. Mater. 2 (1993) 597.
[31] A. Matthews, S.S. Eskildsen, Diamond Relat. Mater. 3 (1994) 902.
[32] A.A. Voevodin, M.S. Donley, Surf. Coat. Technol. 82 (1996) 199.
[33] J. Robertson, Mater. Sci. Eng. R. Rep. 37 (2002) 129.
[34] A.M. WU, J. Sun, X.K. Shen, N. Xu, Z.F. Ying, Z.B. Dong, J.D. Wu, Diamond Relat. Mater. 15 (2006) 1235.
[35] J. Robertson, Prog. Solid. State. Chem. 21 (1991) 199.
[36] Y. Lifshitz, Diamond Relat. Mater. 5 (1996) 388.
[37] A. Hu, I. Alkhesho, H. Zhou, W.W. Duley, Diamond Relat. Mater. 16 (2007) 149.
[38] M.L. Morrison, R.A. Buchanan, P.K. Liaw, C.J. Berry, R.L. Brigmon, L. Riester, H. Abernathy, C. Jin, R.J. Narayan, Diamond Relat. Mater. 15 (2006) 138.
[39] D.S. Knight, W.B. White, J. Mater. Res. 4 (1989) 385.
[40] R. Diamant, E. Jimenez, E. Haro-Poniatowski, L. Ponce, M. Fernandez-Guasti, J.C. Alonso, Diamond Relat. Mater. 8 (1999) 1277.
[41] V.N. Apakina, A.L. Karuzskii, M.S. Kogan, A.V. Kvit, N.N. Melnik, Y.A. Mityagin, V.N. Murzin, A.A. Orlikovsky, A.V. Perestoronin, S.D. Tkachenko, N.A. Volchkov, Diamond Relat. Mater. 6 (1997) 564.
[42] D.R. Tallant, J.E. Parmeter, M.P. Siegal, R.L. Simpson, Diamond Relat. Mater. 4 (1995) 191.
[43] D.T. Peeler, P.T. Murray, Diamond Relat. Mater. 3 (1994) 1124.
[44] J.D. Carey, S.R.P. Silva, Phys. Rev. B 70 (2004) 235417.
[45] M. Chhowalla, A.C. Ferrari, J. Robertson, G.A.J. Amaratunga, Appl. Phys. Lett. 76 (2000) 1419.
[46] A.C. Ferrari, J. Robertson, Phys. Rev. B 61 (2000) 14095.
[47] C. Mapelli, C. Castiglioni, G. Zerbi, K. Mullen, Phys. Rev. B 60 (1999) 12710
[48] R. Tenne, K. Patel, K. Hashimoto, A. Fujishima, J. Electroanal. Chem. 347 (1993) 409.
[49] N. Vinokur, B. Miller, Y. Avyigal, R. Kalish, J. Electrochem. Soc. 143 (1996) L238.
[50] S. Alhashem, F. Chambers, J.W. Stojek, G.M. Swain, R. Ramesham, Anal. Chem. 67 (1995) 2812.
[51] H.B. Martin, A. Argoitia, U. Landau, A.B. Anderson, J.C. Angus, J. Electrochem. Soc. 144 (1996) L133.
[52] G.M. Swain, Adv. Mater. 6 (1994) 388.
[53] Y.V. Pleskov, V.T. Mishuk, M.A. Abaturov, V.V. Elkin, M.D. Krotova, V.P. Varin, I.G. Teremetskaya, J. Electroanal. Chem. 396 (1995) 227.
[54] Y.V. Pleskov, V.V. Elkin, M.A. Abaturov, M.D. Krotova, V.Y. Mishuk, V.P. Varin, I.G. Teremetskaya, J. Electroanal. Chem. 413 (1996) 105.
[55] A.Y. Sakharova, Y.V. Pleskov, F.D. Quarto, S. Piazza, C. Sunseri, I.G. Teremetskaya, V.P. Varin, Russ. J. Electrochem. 31 (1995) 169.
[56] A.Y. Sakharova, A.E. Sevastyanov, Y.V. Pleskov, G.L. Teplitskaya, V.V. Surikov, A.A. Voloshin, Elektrokhimiya 27 (1991) 263.
[57] B. Tomcik, S.C. Seng, B. Balakoisnan, J.Y. Lee, Diamond Relat. Mater. 11 (2002) 1409.
[58] S. Zhang, P. Hing, J. Gao, Diamond Relat. Mater. 11 (2002) 160.
[59] Edwards, Vacum products catalogue (1996–1997) (1995) 239.
[60] R.F. Xiao, Appl. Phys. Lett. 67 (1995) 1022.

[61] R.F. Xiao, Appl Phys Lett 67 (1995) 3117.
[62] G. Nurk, A. Jänes, K. Lust, E. Lust, J. Electroanal. Chem. 515 (2001) 17.
[63] E. Lust, A. Jänes, V. Sammelselg, P. Miidla, K. Lust, Electrochim. Acta. 43 (1998) 373.
[64] E. Lust, A. Jänes, V. Sammelselg, P. Miidla, Electrochim. Acta. 46 (2000) 185.
[65] E. Lust, A. Jänes, K. Lust, V. Sammelselg, P. Miidla, Electrochim. Acta. 42 (1997) 2861.
[66] S. Leppävuori, J. Levoska, J. Vaara, O. Kusmartseva, Mater. Res. Soc. Symp. Proc. 285 (1993) 557.
[67] Y. Lifshitz, G.D. Lempert, E. Grossman, I. Avigal, C. Uzan Saguy, R. Kalish, J. Kulik, D. Marton, J.W. Rabalais, Diamond Relat. Mater. 4 (1995) 318.
[68] P.V. Huong, J. Mol. Struct. 292 (1993) 81.
[69] S. E. Johnson, M.N.R. Ashfold, M.P. Knapper, R.J. Lade, K.N. Rosser, N A. Fox, W.N. Wang, Diamond Rel. Mat. 6 (1997) 569.
[70] M.L. Terranova, V. Sessa, S. Piccirillo, Appl. Phys. Lett. 75 (1999) 379.
[71] J. Choi, S. Miyagawaa, S. Nakaoa, M. Ikeyamaa, Y. Miyagawa, Diamond Relat. Mater. 15 (2006) 948.
[72] N. Yasumaru, K. Miyazaki, J. Kiuchi, Appl. Surf. Sci. 254 (2008) 2364.
[73] E. Cappelli, C. Scilletta, S. Orlando, R. Flammini, S. Iacobucci, P. Ascarelli, Thin Solid Films 482 (2005) 305.
[74] J.R. MacDonald, Impedance spectroscopy: emphasizing solid materials and systems. Wiley, New York (1987).
[75] R. de Levie, J. Electroanal. Chem. 281 (1990) 1.
[76] J.R. MacDonald, Solid State Ionics 13 (1989) 147.
[77] L. Nyikos, T. Pajkossy, Electrochim. Acta. 31 (1986) 1347.
[78] P. Liu, H. Wu, Solid State Ionics 92 (1996) 91.
[79] M. Doyle, J.P. Meyers, J. Newman, J. Electrochem Soc. 147 (2000) 99.
[80] J.P. Meyers, M. Doyle, R.M. Darling, J. Newman, J. Electrochem. Soc. 147 (2000) 293.
[81] U. Rammelt, G. Reinhard, K. Rammelt, J. Electroanal. Chem. 180 (1984) 327.
[82] J. Tanguy, N. Mermilliod, M. Hoclet, J. Electrochem. Soc. 134 (1987) 795.
[83] G. Paasch, K. Micka, M. Schwarzenberg, K. Jobst, L. Sawtschenko, Electrochim. Acta. 37 (1992) 2453.
[84] G. Paasch, K. Micka, P. Gersdorf, Electrochim. Acta. 38 (1993) 2653.
[85] C. Ho, D. Raistrick, R. Huggins, J. Electrochem. Soc. 137 (1980) 343.
[86] J.R. MacDonald, Ann. Biomed. Eng. 20 (1992) 289.
[87] T. Jacobsen, K. West, Electrochim. Acta. 40 (1995) 233.
[88] A.N. Frumkin, Melik-Gaikazyan, VI Dokl. Akad. Nauk. SSSR 77 (1951) 855.
[89] Melik-Gaikazyan, VI Zh. Fiz. Khim. 26 (1952) 560.
[90] J.P. Randin, E. Yeager, J. Electroanal. Chem. 36 (1972) 257.
[91] H. Gerisher, J. Phys. Chem. 89 (1985) 4249.
[92] H. Gerisher, R. McInture, D. Sherson, W. Strock, J. Phys. Chem. 91 (1987) 1930.
[93] L.I. Daikhin, A.A. Kornyshev, M. Urbakh, Electrochim. Acta. 42 (1997) 2853.
[94] L.I. Daikhin, A.A. Kornyshev, M. Urbakh, J. Chem. Phys. 108 (1998) 171.

# 9. SUMMARY IN ESTONIAN

## Õhukeste teemandisarnaste süsiniku kilede süntees impulss-laser sadestus meetodil ja nende karakteriseerimine

Käesolevas töös sünteesiti erinevaid süsiniku kilesid, kasutades selleks nelja erineva aparatuuri konfiguratsiooni. Sünteesitud kilede karakteriseerimiseks kasutati optilist mikroskoopiat, Raman spektroskoopiat, aatomjõu mikroskoopiat ja elektrokeemilisi mõõtmismeetoteid.

Miniatuurses lasersadestus kambris sünteesitud süsiniku kilede Raman spektroskoopia andmed näitavad, et kiled, mis on kasvanud $H_2O_2$ voolus (0.02 – 1.2 mbar), on kõrgema $sp^3$ hübridisatsioonis oleva sideme sisaldusega (hinnatav keskmine $sp^3/sp^2$ sidemete suhe on > 50%). Nende kilede optilise mikroskoopia uuringud näitavad, et kilede piirkonnad, mis on kasvanud kindla energiatihedusega eksimeerlaseri kiirguses, on tugevalt interferents värvilised. Selline värviliste osakesete piirkond on suureks kontrastiks, ilma laserkiirituseta kasvanud, hallile ja pruunile piirkonnale ning näitab ühtlasi, et laseri kiirguses võivad kasvada väga laia keelutsooni laiusega ($\Delta E > 3$ eV) teemandisarnased süsiniku kiled. Aatomjõu mikroskoopia mõõtmised näitavad, et laseri kiirguses kasvanud teemandisarnased süsiniku kiled on siledamad, kuid eriti siledaid pindasid on täheldatud neis piirkondades esinevatel värvilistel osakestel.

Raman spektroskoopia uuringud näitasid, et kõrgema energiatihedusega laseri kiirgus omab positiivset mõju $sp^3$ hübridisatsioonis olevate süsiniku sidemete moodustamisel. $H_2O_2$ lisandi mõju kasvavatele süsiniku kilede struktuurile võib kirjeldada kui korrapäraste aromaatsete süsiniku ringide arvu kasvuga koos aromaatsete klastrite suuruse vähenemisega kiles. Raman spektroskoopia tulemused kinnitasid ka G joone liikumist suuremate sageduste poole kõrgemate kasvatusaluse temperatuuride korral, mis näitab $sp^3$ hübridisatsioonis oleva süsiniku transformeerumist $sp^2$ hübridisatsioonis olevaks süsinikuks. G joone nihke sõltuvus Raman spektris kasvatusaluse temperatuurist on ligilähedaselt lineaarne. Aatomjõu mikroskoopia uuringud näitasid, et madalama kasvatusaluse temperatuuri tulemuseks on suurema teralise pinna tekkimine. Suurimat ruutkeskmise pinnakareduse väärtuse muutust täheldati suhteliselt kitsas temperatuuride vahemikus sünteesitud kiledel (50–100ºC), millest kõrgematel sadestustemperatuuridel ruutkeskmise pinnakareduse väärtuse vähenemine aeglustus ning karedusfaktor hakkas lähenema platoole.

Raman spektroskoopia uuringu tulemused näitasid, et kasvatusaluse kiiritamine sadestustsüklite vahel täpselt kontrollitud energiatihedusega laseri kiirega võimaldab tekitada teemandi sarnases süsiniku struktuuris individuaalset teemandi faasi. Teemandi faasi tekkimine leiab aset kiiritava laseri kiire väga kitsas energiatiheduse vahemikus, mis samas on energeetiliselt väga lähedal süsiniku struktuuri grafitiseerimisele. Leiti, et kõrgematel energiatihedustel leiabki aset samaaegselt teemandi faasi tekkimisega ka olemasoleva teemandi sarnase süsiniku grafitiseerumine.

Tsüklilise voltamperomeetria ja elektrokeemilise impetantsi andmed näitasid, et DLCE|*x*M NaF+$H_2O$ süsteem on peaaegu ideaalselt polariseeritav potentsiaalide vahemikus –0.4 < E < 1.1 V [vs. AgCl|Ag (sat. KCl in $H_2O$)]. Aatomjõu mikroskoopia andmed näitasid, et teemandi sarnase süsinikelektroodi ruutkeskmine pinnakaredus on 81 Å ja pinnal olevate osakeste keskmine suurus oli 0.1 µm. Mõõdetud elektrokeemilise impedantsi graafiku kuju sõltub elektroodi potentsiaalist ja elektrolüüdi kontsentratsioonist. Eksperimendi andmete mittelineaarne vähimruutude lähendusmeetod näitab, et erinevad ekvivalentskeemid on kasutatavad eksperimentaalsete kompleksimpedantsi sõltuvuste modelleerimiseks. Parim kokkulangevus on saavutatud modelleerimisel ekvivalent skeemiga, mis on kombineeritud elektroodi süsteemi kogutakistusest $R_{el}$, (sisaldab kogu teemandi sarnase süsiniku kile ja kogu elektrolüüdi lahuse takistust) kile pindkihi mahtuvusest $C_1$ ja pindkihi takistusest $R_3$, kaksikkihi mahtuvusest $C_2$, osalisest või ”tõelisest” faradi reaktsiooni iseloomustavast takistusest $R_2$, adsorptsioonilisest mahtuvusest $C_3$ ja Warburgi difusioonilisest impetantsist $Z_w$.

# 10. ACKNOWLEDGEMENTS

I wish to express my greatest gratitude to my supervisors Professor Enn Lust and Raivo Jaaniso for assistance and scientific guidance trough the many years.

I would like to thank Richard Gymer for the measurements opportunity in Cavendish laboratory, University of Cambridge.

Special thanks to Tea Avarmaa and colleagues for the patience.

I would also like to thank Alar Jänes for the some problems dissolves.

Last, but not least, I should like to thank my mother for the many-sided support.

# 11. PUBLICATIONS

# CURRICULUM VITAE


| | |
|---|---|
| Given name and surname: | Jaanus Eskusson |
| Date and place of birth: | 24.01.1977, Pärnu |
| Citizenchip: | Estonian |
| Address: | Institute of Chemistry<br>University of Tartu<br>2 Jakobi St., Tartu 51014, Estonia |
| E-mail address: | jaanus.eskusson@ut.ee |


## Education

| | |
|---|---|
| 2002–… | University of Tartu, *Ph.D.* student (physical and electrochemistry) |
| 2000–2002 | University of Tartu, *M.Sc.* in physical and electrochemistry |
| 1996–2000 | University of Tartu, *B.Sc.* in chemistry |
| 1993–1995 | Pärnu 2. secondary school |

## Schooling

| | |
|---|---|
| 2003 | Technology Transfer 2003, IBM Business Consulting Services |
| 2003 | 34th IFF Fundamentals of Nanoelectronics, Juelich, German |
| 2002 | Thin Film Deposition and Applications, Uppsala, Sweden |

## Professional employment

| | |
|---|---|
| 2007– | University of Tartu, Institute of Chemistry, extraordinary researcher |
| 2003–2005 | University of Tartu, Institute of Technology, project manager |
| 2000–2004 | University of Tartu, Institute of Physics, engineer |
| 1997–2000 | Institute of Physics, laboratoorian |

## List of publications


1. T. Avarmaa, T. Jantson, J. Eskusson, R. Jaaniso, SPM characterized Er: YAG and DLC films prepared by pulsed laser deposition, Abstr. of Nordic-Baltic SPM Workshop, Marstrand, Sweden, (2000).
2. T. Jantson, T. Avarmaa, H. Mändar, J. Eskusson, A. Lõhmus, R. Jaaniso, Er:YAG thin films and nanocrystals prepared by pulsed laser deposition, SPIE Proc. 4318 (2001) 36–41.

3. T. Jantson, J. Eskusson, H. Mändar, T. Avarmaa, R. Jaaniso, Structure-morphology relations of laser deposited Er:YAG and DLC thin films, Abstr. of Nordic-Baltic SPM Workshop, Tartu, Estonia, (2002).
4. K. Saal, A. Lohmus, R. Lohmus, J. Eskusson, R. Jaaniso, A. Metspalu, A. Kurg, AFM studies on oligomeric DNA immobilized on mica carrier, Abstr. of Nordic-Baltic SPM Workshop, Tartu, Estonia (2002).
5. K. Saal, A. Lohmus, R. Lohmus, J. Eskusson, R. Jaaniso, A. Metspalu, A. Kurg, AFM studies on oligomeric DNA immobilized on mica carrier, Abstr. of 7th international conference on nanometer-scale acience and tech-nolocy + 21st european conference on surface science NANO-7/ECOSS-21, Malmö, Sweden (2002).
6. E. Lust, A. Jänes, G. Nurk, K. Laes, S. Kallip, V. Sammelselg, J. Eskusson, R. Jaaniso, K. Lust, Adsorption kinetics of various molecules and ions on the bismuth single crystal and nanostructured carbon electrodes, Abstr. of ISE 53rd Ann. Meet., Düsseldorf (2002).
7. G. Nurk, J. Eskusson, R. Jaaniso, E. Lust, Electrochemical properties of diamond-like carbon electrodes prepared by pulsed laser deposition method, J. Solid State Electrochem., 7 (2003) 421–434.
8. J. Eskusson, R. Jaaniso, T. Avarmaa, T. Jantson, E Lust, Synthesis of diamond-like carbon films by pulsed laser deposition in a tiny vacuum chamber, SPIE Proc., 6591 (2007) 65910L.
9. J. Eskusson, R. Jaaniso, E. Lust, Synthesis of DLC films by PLD from liquid target and dependence of film properties on the synthesis conditions, Appl. Phys. A (2008) 745.
10. J. Eskusson, R. Jaaniso, E. Lust, Diamond-like carbon films prepared by periodic pulsed laser deposition and laser irradiation, Microelectronics, MEMS and Nanotechnology 2007, Canberra, ACT, Australia, (2007).
11. J. Eskusson, P. Möller, R. Jaaniso, Electrochemical properties of Nd-doped diamond-like carbon electrodes prepared by pulsed laser deposition method, 5th Baltic Conference on Electrochemistry, Tartu, Estonia, (2008).
12. J. Eskusson, R. Jaaniso, E. Lust, Diamond-like phase formation in an amorphous carbon films prepared by periodic pulsed laser deposition and laser irradiation method, Appl. Surf. Sci., (2009).

# ELULOOKIRJELDUS


| | |
|---|---|
| Ees-ja perekonnanimi: | Jaanus Eskusson |
| Sünniaeg ja koht: | 24.01.1977, Pärnu |
| Kodakondsus: | Eesti |
| Aadress: | Keemia Instituut<br>Tartu Ülikool<br>Jakobi 2, Tartu 51014, Eesti |
| E-mail: | jaanus.eskusson@ut.ee |


## Haridus

| | |
|---|---|
| 2002–… | Tartu Ülikool, Loodus- ja tehnoloogiadeaduskond, doktorant füüsikalise ja elektrokeemia erialal |
| 2000–2002 | Tartu Ülikool, Füüsika-keemiateaduskond, *M.Sc.* füüsikalise ja elektrokeemia erialal |
| 1996–2001 | Tartu Ülikool, Füüsika-keemiateaduskond, *B.Sc.* Keemia erialal |
| 1993–1995 | Pärnu 2. keskkool |

## Koolitus

| | |
|---|---|
| 2003 | Technology Transfer 2003, IBM Business Consulting Services |
| 2003 | 34th IFF Fundamentals of Nanoelectronics, Juelich, German |
| 2002 | Thin Film Deposition and Applications, Uppsala, Sweden |

## Teenistuskäik

| | |
|---|---|
| 2007– | Tartu Ülikool, Keemia Instituut, erakorraline teadur |
| 2003–2005 | Tartu Ülikool, Tehnoloogiainstituut, projektijuht |
| 2000–2004 | Tartu Ülikool, Füüsika instituut, insener |
| 1997–2000 | Füüsika Instituut, laborant |

## Ilmunud teaduspublikatsioonid


1. T. Avarmaa, T. Jantson, J. Eskusson, R. Jaaniso, SPM characterized Er:YAG and DLC films prepared by pulsed laser deposition, Abstr. of Nordic-Baltic SPM Workshop, Marstrand, Sweden, (2000).
2. T. Jantson, T. Avarmaa, H. Mändar, J. Eskusson, A. Lõhmus, R. Jaaniso, Er:YAG thin films and nanocrystals prepared by pulsed laser deposition, SPIE Proc. 4318 (2001) 36–41.

3. T. Jantson, J. Eskusson, H. Mändar, T. Avarmaa, R. Jaaniso, Structure-morphology relations of laser deposited Er:YAG and DLC thin films, Abstr. of Nordic-Baltic SPM Workshop, Tartu, Estonia, (2002).
4. K. Saal, A. Lohmus, R. Lohmus, J. Eskusson, R. Jaaniso, A. Metspalu, A. Kurg, AFM studies on oligomeric DNA immobilized on mica carrier, Abstr. of Nordic-Baltic SPM Workshop, Tartu, Estonia (2002).
5. K. Saal, A. Lohmus, R. Lohmus, J. Eskusson, R. Jaaniso, A. Metspalu, A. Kurg, AFM studies on oligomeric DNA immobilized on mica carrier, Abstr. of 7th international conference on nanometer-scale acience and tech-nolocy + 21st european conference on surface science NANO-7/ECOSS-21, Malmö, Sweden (2002).
6. E. Lust, A. Jänes, G. Nurk, K. Laes, S. Kallip, V. Sammelselg, J. Eskusson, R. Jaaniso, K. Lust, Adsorption kinetics of various molecules and ions on the bismuth single crystal and nanostructured carbon electrodes, Abstr. of ISE 53rd Ann. Meet., Düsseldorf (2002).
7. G. Nurk, J. Eskusson, R. Jaaniso, E. Lust, Electrochemical properties of diamond-like carbon electrodes prepared by pulsed laser deposition method, J. Solid State Electrochem., 7 (2003) 421–434.
8. J. Eskusson, R. Jaaniso, T. Avarmaa, T. Jantson, E Lust, Synthesis of diamond-like carbon films by pulsed laser deposition in a tiny vacuum chamber, SPIE Proc., 6591 (2007) 65910L.
9. J. Eskusson, R. Jaaniso, E. Lust, Synthesis of DLC films by PLD from liquid target and dependence of film properties on the synthesis conditions, Appl. Phys. A (2008) 745.
10. J. Eskusson, R. Jaaniso, E. Lust, Diamond-like carbon films prepared by periodic pulsed laser deposition and laser irradiation, Microelectronics, MEMS and Nanotechnology 2007, Canberra, ACT, Australia, (2007).
11. J. Eskusson, P. Möller, R. Jaaniso, Electrochemical properties of Nd-doped diamond-like carbon electrodes prepared by pulsed laser deposition method, 5th Baltic Conference on Electrochemistry, Tartu, Estonia, (2008).
12. J. Eskusson, R. Jaaniso, E. Lust, Diamond-like phase formation in an amorphous carbon films prepared by periodic pulsed laser deposition and laser irradiation method, Appl. Surf. Sci., (2009).

# DISSERTATIONES CHIMICAE UNIVERSITATIS TARTUENSIS

1. **Toomas Tamm.** Quantum-chemical simulation of solvent effects. Tartu, 1993, 110 p.
2. **Peeter Burk.** Theoretical study of gas-phase acid-base equilibria. Tartu, 1994, 96 p.
3. **Victor Lobanov.** Quantitative structure-property relationships in large descriptor spaces. Tartu, 1995, 135 p.
4. **Vahur Mäemets.** The $^{17}O$ and $^{1}H$ nuclear magnetic resonance study of $H_2O$ in individual solvents and its charged clusters in aqueous solutions of electrolytes. Tartu, 1997, 140 p.
5. **Andrus Metsala.** Microcanonical rate constant in nonequilibrium distribution of vibrational energy and in restricted intramolecular vibrational energy redistribution on the basis of slater's theory of unimolecular reactions. Tartu, 1997, 150 p.
6. **Uko Maran.** Quantum-mechanical study of potential energy surfaces in different environments. Tartu, 1997, 137 p.
7. **Alar Jänes.** Adsorption of organic compounds on antimony, bismuth and cadmium electrodes. Tartu, 1998, 219 p.
8. **Kaido Tammeveski.** Oxygen electroreduction on thin platinum films and the electrochemical detection of superoxide anion. Tartu, 1998, 139 p.
9. **Ivo Leito.** Studies of Brønsted acid-base equilibria in water and non-aqueous media. Tartu, 1998, 101 p.
10. **Jaan Leis.** Conformational dynamics and equilibria in amides. Tartu, 1998, 131 p.
11. **Toonika Rinken.** The modelling of amperometric biosensors based on oxidoreductases. Tartu, 2000, 108 p.
12. **Dmitri Panov.** Partially solvated Grignard reagents. Tartu, 2000, 64 p.
13. **Kaja Orupõld.** Treatment and analysis of phenolic wastewater with microorganisms. Tartu, 2000, 123 p.
14. **Jüri Ivask.** Ion Chromatographic determination of major anions and cations in polar ice core. Tartu, 2000, 85 p.
15. **Lauri Vares.** Stereoselective Synthesis of Tetrahydrofuran and Tetrahydropyran Derivatives by Use of Asymmetric Horner-Wadsworth-Emmons and Ring Closure Reactions. Tartu, 2000, 184 p.
16. **Martin Lepiku.** Kinetic aspects of dopamine $D_2$ receptor interactions with specific ligands. Tartu, 2000, 81 p.
17. **Katrin Sak.** Some aspects of ligand specificity of P2Y receptors. Tartu, 2000, 106 p.
18. **Vello Pällin.** The role of solvation in the formation of iotsitch complexes. Tartu, 2001, 95 p.

19. **Katrin Kollist.** Interactions between polycyclic aromatic compounds and humic substances. Tartu, 2001, 93 p.
20. **Ivar Koppel.** Quantum chemical study of acidity of strong and superstrong Brønsted acids. Tartu, 2001, 104 p.
21. **Viljar Pihl.** The study of the substituent and solvent effects on the acidity of OH and CH acids. Tartu, 2001, 132 p.
22. **Natalia Palm.** Specification of the minimum, sufficient and significant set of descriptors for general description of solvent effects. Tartu, 2001, 134 p.
23. **Sulev Sild.** QSPR/QSAR approaches for complex molecular systems. Tartu, 2001, 134 p.
24. **Ruslan Petrukhin.** Industrial applications of the quantitative structure-property relationships. Tartu, 2001, 162 p.
25. **Boris V. Rogovoy.** Synthesis of (benzotriazolyl)carboximidamides and their application in relations with *N*- and *S*-nucleophyles. Tartu, 2002, 84 p.
26. **Koit Herodes.** Solvent effects on UV-vis absorption spectra of some solvatochromic substances in binary solvent mixtures: the preferential solvation model. Tartu, 2002, 102 p.
27. **Anti Perkson.** Synthesis and characterisation of nanostructured carbon. Tartu, 2002, 152 p.
28. **Ivari Kaljurand.** Self-consistent acidity scales of neutral and cationic Brønsted acids in acetonitrile and tetrahydrofuran. Tartu, 2003, 108 p.
29. **Karmen Lust.** Adsorption of anions on bismuth single crystal electrodes. Tartu, 2003, 128 p.
30. **Mare Piirsalu.** Substituent, temperature and solvent effects on the alkaline hydrolysis of substituted phenyl and alkyl esters of benzoic acid. Tartu, 2003, 156 p.
31. **Meeri Sassian.** Reactions of partially solvated Grignard reagents. Tartu, 2003, 78 p.
32. **Tarmo Tamm.** Quantum chemical modelling of polypyrrole. Tartu, 2003. 100 p.
33. **Erik Teinemaa.** The environmental fate of the particulate matter and organic pollutants from an oil shale power plant. Tartu, 2003. 102 p.
34. **Jaana Tammiku-Taul.** Quantum chemical study of the properties of Grignard reagents. Tartu, 2003. 120 p.
35. **Andre Lomaka.** Biomedical applications of predictive computational chemistry. Tartu, 2003. 132 p.
36. **Kostyantyn Kirichenko.** Benzotriazole — Mediated Carbon–Carbon Bond Formation. Tartu, 2003. 132 p.
37. **Gunnar Nurk.** Adsorption kinetics of some organic compounds on bismuth single crystal electrodes. Tartu, 2003, 170 p.
38. **Mati Arulepp.** Electrochemical characteristics of porous carbon materials and electrical double layer capacitors. Tartu, 2003, 196 p.
39. **Dan Cornel Fara.** QSPR modeling of complexation and distribution of organic compounds. Tartu, 2004, 126 p.

40. **Riina Mahlapuu.** Signalling of galanin and amyloid precursor protein through adenylate cyclase. Tartu, 2004, 124 p.
41. **Mihkel Kerikmäe.** Some luminescent materials for dosimetric applications and physical research. Tartu, 2004, 143 p.
42. **Jaanus Kruusma.** Determination of some important trace metal ions in human blood. Tartu, 2004, 115 p.
43. **Urmas Johanson.** Investigations of the electrochemical properties of polypyrrole modified electrodes. Tartu, 2004, 91 p.
44. **Kaido Sillar.** Computational study of the acid sites in zeolite ZSM-5. Tartu, 2004, 80 p.
45. **Aldo Oras.** Kinetic aspects of dATPαS interaction with $P2Y_1$ receptor. Tartu, 2004, 75 p.
46. **Erik Mölder.** Measurement of the oxygen mass transfer through the air-water interface. Tartu, 2005, 73 p.
47. **Thomas Thomberg.** The kinetics of electroreduction of peroxodisulfate anion on cadmium (0001) single crystal electrode. Tartu, 2005, 95 p.
48. **Olavi Loog.** Aspects of condensations of carbonyl compounds and their imine analogues. Tartu, 2005, 83 p.
49. **Siim Salmar.** Effect of ultrasound on ester hydrolysis in aqueous ethanol. Tartu, 2006, 73 p.
50. **Ain Uustare.** Modulation of signal transduction of heptahelical receptors by other receptors and G proteins. Tartu, 2006, 121 p.
51. **Sergei Yurchenko.** Determination of some carcinogenic contaminants in food. Tartu, 2006, 143 p.
52. **Kaido Tämm.** QSPR modeling of some properties of organic compounds. Tartu, 2006, 67 p.
53. **Olga Tšubrik.** New methods in the synthesis of multisubstituted hydrazines. Tartu. 2006, 183 p.
54. **Lilli Sooväli.** Spectrophotometric measurements and their uncertainty in chemical analysis and dissociation constant measurements. Tartu, 2006, 125 p.
55. **Eve Koort.** Uncertainty estimation of potentiometrically measured ph and $pK_a$ values. Tartu, 2006, 139 p.
56. **Sergei Kopanchuk.** Regulation of ligand binding to melanocortin receptor subtypes. Tartu, 2006, 119 p.
57. **Silvar Kallip.** Surface structure of some bismuth and antimony single crystal electrodes. Tartu, 2006, 107 p.
58. **Kristjan Saal.** Surface silanization and its application in biomolecule coupling. Tartu, 2006, 77 p.
59. **Tanel Tätte.** High viscosity $Sn(OBu)_4$ oligomeric concentrates and their applications in technology. Tartu, 2006, 91 p.
60. **Dimitar Atanasov Dobchev**. Robust QSAR methods for the prediction of properties from molecular structure. Tartu, 2006, 118 p.

61. **Hannes Hagu**. Impact of ultrasound on hydrophobic interactions in solutions. Tartu, 2007, 81 p.
62. **Rutha Jäger.** Electroreduction of peroxodisulfate anion on bismuth electrodes. Tartu, 2007, 142 p.
63. **Kaido Viht.** Immobilizable bisubstrate-analogue inhibitors of basophilic protein kinases: development and application in biosensors. Tartu, 2007, 88 p.
64. **Eva-Ingrid Rõõm.** Acid-base equilibria in nonpolar media. Tartu, 2007, 156 p.
65. **Sven Tamp.** DFT study of the cesium cation containing complexes relevant to the cesium cation binding by the humic acids. Tartu, 2007, 102 p.
66. **Jaak Nerut.** Electroreduction of hexacyanoferrate(III) anion on Cadmium (0001) single crystal electrode. Tartu, 2007, 180 p.
67. **Lauri Jalukse.** Measurement uncertainty estimation in amperometric dissolved oxygen concentration measurement. Tartu, 2007, 112 p.
68. **Aime Lust.** Charge state of dopants and ordered clusters formation in $CaF_2$:Mn and $CaF_2$:Eu luminophors. Tartu, 2007, 100 p.
69. **Iiris Kahn**. Quantitative Structure-Activity Relationships of environmentally relevant properties. Tartu, 2007, 98 p.
70. **Mari Reinik.** Nitrates, nitrites, N-nitrosamines and polycyclic aromatic hydrocarbons in food: analytical methods, occurrence and dietary intake. Tartu, 2007, 172 p.
71. **Heili Kasuk.** Thermodynamic parameters and adsorption kinetics of organic compounds forming the compact adsorption layer at Bi single crystal electrodes. Tartu, 2007, 212 p.
72. **Erki Enkvist.** Synthesis of adenosine-peptide conjugates for biological applications. Tartu, 2007, 114 p.
73. **Svetoslav Hristov Slavov**. Biomedical applications of the QSAR approach. Tartu, 2007, 146 p.
74. **Eneli Härk.** Electroreduction of complex cations on electrochemically polished Bi(*hkl*) single crystal electrodes. Tartu, 2008, 158 p.
75. **Priit Möller.** Electrochemical characteristics of some cathodes for medium temperature solid oxide fuel cells, synthesized by solid state reaction technique. Tartu, 2008, 90 p.
76. **Signe Viggor.** Impact of biochemical parameters of genetically different pseudomonads at the degradation of phenolic compounds. Tartu, 2008, 122 p.
77. **Ave Sarapuu.** Electrochemical reduction of oxygen on quinone-modified carbon electrodes and on thin films of platinum and gold. Tartu, 2008, 134 p.
78. **Agnes Kütt.** Studies of acid-base equilibria in non-aqueous media. Tartu, 2008, 198 p.
79. **Rouvim Kadis.** Evaluation of measurement uncertainty in analytical chemistry: related concepts and some points of misinterpretation. Tartu, 2008, 118 p.

80. **Valter Reedo.** Elaboration of IVB group metal oxide structures and their possible applications. Tartu, 2008, 98 p.
81. **Aleksei Kuznetsov.** Allosteric effects in reactions catalyzed by the cAMP-dependent protein kinase catalytic subunit. Tartu, 2009, 133 p.
82. **Aleksei Bredihhin.** Use of mono- and polyanions in the synthesis of multisubstituted hydrazine derivatives. Tartu, 2009, 105 p.
83. **Anu Ploom.** Quantitative structure-reactivity analysis in organosilicon chemistry. Tartu, 2009, 99 p.
84. **Argo Vonk.** Determination of adenosine $A_{2A}$- and dopamine $D_1$ receptor-specific modulation of adenylate cyclase activity in rat striatum. Tartu, 2009, 129 p.
85. **Indrek Kivi.** Synthesis and electrochemical characterization of porous cathode materials for intermediate temperature solid oxide fuel cells. Tartu, 2009, 177 p.